Temporal leakage in annual satellite embeddings inflates landslide susceptibility assessments

Yifan Du*, https://orcid.org/0009-0008-7740-5408
Tianhe Zheng, https://orcid.org/0009-0000-8993-814X
Peiyan Yang, https://orcid.org/0009-0004-6214-0831
Yibo Li, https://orcid.org/0009-0002-2926-757X
Junhang Zhou, https://orcid.org/0009-0002-0458-2127
Kun Yang, https://orcid.org/0009-0006-6609-219X

North China University of Water Resources and Electric Power, 136 Jinshui East Road, Zhengzhou 450046, Henan, China

*Corresponding author: Yifan Du, duyifan619916@gmail.com

This manuscript is a preprint and has not been peer reviewed. It has been submitted to *Journal of Remote Sensing*. Subsequent versions may differ. Code, analysis log and derived data: https://doi.org/10.5281/zenodo.23467611.

Abstract

Annual satellite embeddings summarize a calendar year, so the layer for a landslide's event year can also record the event's aftermath. We quantified how this input timing biases susceptibility evaluation across 18 events and 61,402 landslide locations, changing only the input year while samples, spatial folds and models stayed fixed. Event-year AlphaEarth inputs raised within-event AUC by 0.0874 (95% confidence interval 0.0649–0.1098) for a point model and by 0.0705 (0.0475–0.0934) for a patch model. The point increment remained 0.085 after pre-event drift correction. TESSERA and radiometrically audited annual Sentinel-2 point composites also showed positive average increments. The bias depended on the workflow and arose mainly when training and testing shared event-year inputs. Controlled Sentinel-2 experiments used three dates per input; moving the window end from 1 day before to 60 days after the event raised AUC by 0.423 and 0.231 more than the same shift in the preceding year. Input timing also changed map rankings: in nine mapped domains, the highest-scoring 10% of area captured about 21–22 percentage points more landslide area, and the direction held over two entire municipalities. In retrospective tests that respected observation time, pre-event embeddings kept regional value. Beyond conventional factors and explicit landslide history, they added 0.059 AUC in North Carolina and 0.008 in Lushan, where the interval included zero. Spatial cross-validation alone does not control predictor timing. We release an audit that links observation windows, target dates, training histories and map domains.

Keywords: temporal leakage; annual satellite embeddings; landslide susceptibility; remote sensing validation; AlphaEarth Foundations; TESSERA

Introduction

Annual satellite embeddings now connect large Earth-observation archives to downstream environmental models. AlphaEarth Foundations (AEF) compresses multisensor observations into a 64-dimensional vector per 10 m pixel and calendar year, and TESSERA represents Sentinel-1 and Sentinel-2 time series in 128 dimensions [1,2]. Both products are global and free, and they were quickly adopted for landslide mapping and susceptibility [3–6] and for other hazards [7–9]. Their compactness spares users the processing of individual

acquisitions, but it also hides the observation timeline. An embedding labelled with the year of a landslide event can describe both the susceptible terrain and the surface that the landslides left behind.

This creates a validation problem for event-based prediction. Susceptibility models are calibrated on mapped landslides and are increasingly built with machine learning [10,11], and the resulting maps support zoning for land-use planning [12]. Spatial blocking separates training and test locations and reduces the optimism caused by spatial dependence [13–16]. Training on earlier failures separates the chronology of the labels [17,18]. Predictors need a third, separate constraint: observations of the target event's consequences must not enter an evaluation of the ability to anticipate that event. Without it, a model can receive evidence about held-out failures even when the spatial split is rigorous. Annual aggregation gives this kind of leakage a plausible year label and an easy route into routine model comparisons [19,20].

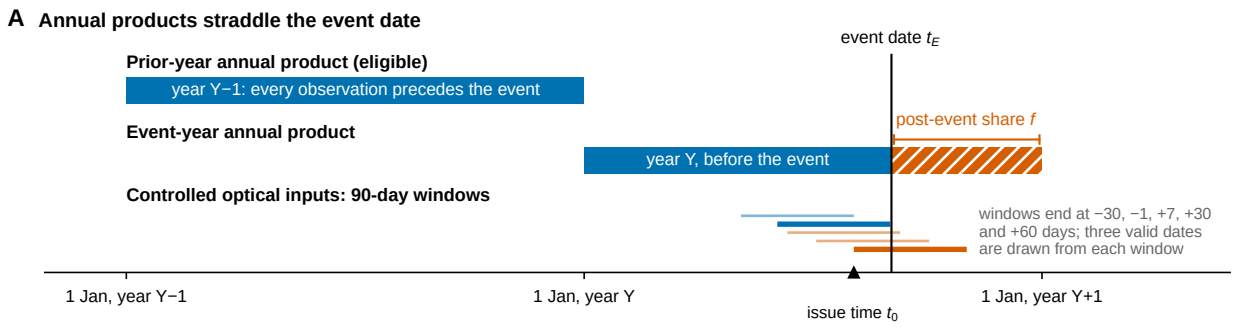
The problem has precedents. Steger et al. [21] showed how post-failure terrain can affect data-driven susceptibility models. Annual embeddings extend the issue to learned, multimodal descriptions of the surface, in which the contribution of each acquisition can no longer be inspected. In a small targeted survey, three of the four studies whose input years could be checked used embeddings that included the event year or later years [3,5,9] (Supplementary Text S5). Fang et al. [4] instead used previous-year embeddings in Taiwan with temporal and spatial holdouts. Still unknown are the size of input-time effects across events and representations, the workflows in which they arise, and their consequences for susceptibility maps and for estimates of added predictive value.

We address these questions with a paired audit of 18 landslide events and make three contributions. First, we quantify the evaluation bias that annual input timing introduces across events and products (AEF, TESSERA and Sentinel-2 composites). The audit holds samples, spatial folds and models fixed, controls for pre-event drift and adds controlled optical observation windows. Second, we show that the bias depends on the modelling workflow and that it changes which areas rank highly under a fixed map area budget. Third, we estimate in retrospective tests how much predictive value pre-event embeddings retain beyond conventional factors and explicit landslide history. We also release the audit materials (code, per-sample predictions, date selections and provenance tables) for reuse.

Materials and Methods

Temporal design and audit logic

Figure 1 summarizes the design. Let t0 be the time at which a prediction is issued and tE the time of the target event. An input is observation-consistent when its observations end no later than t0 and t0 < tE. We distinguish three designs (Fig. 1B). A within-event audit swaps the input year while the labels of one event stay fixed. A retrospective forward test trains on earlier occurrences and uses observations made before the target. Historical deployment additionally requires that products, encoders and confirmed training records were available at t0. Our experiments address the first two designs.



B **Validation designs and what each can show**

Design	Training labels	Inputs	Question answered	This study
Within-event audit	Same event, spatial folds	Annual layer of year Y−1 or Y (year swapped)	How much input time changes the score of one evaluation	Figs. 2–5
Retrospective forward test	Earlier landslides only	Observations made before the target event	What information exists before the target	Fig. 6
Historical deployment	Records confirmed by t_0	Products and encoders released by t_0	Whether a forecast could have been issued at t_0	Not attempted

C **Evidence chain**

18-event paired year swap (Fig. 2) → Fixed-count optical windows (Fig. 3) → Workflow and product checks (Fig. 4) → Map ranking at a fixed area budget (Fig. 5) → Pre-event value beyond history (Fig. 6)

Fig. 1. Temporal audit design. (A) A calendar-year product for the event year Y contains observations made after the event date tE; the hatched part is the post-event share f. The prior-year product ends before tE. The controlled optical inputs use 90-day windows that end at fixed offsets from tE. (B) Three validation designs, the information each may use and the question each can answer. Raw-observation cutoff, product and encoder availability and inventory chronology are separate parts of the information available to a model; this study implements the first two designs. (C) The chain of analyses and the figures that report them.

The primary audit asks how the input year changes the discrimination of the same held-out event labels. The retrospective tests ask how well earlier landslides and pre-target observations discriminate a later event. AEF was released on 30 July 2025 [22], so its earlier annual layers are used retrospectively. The temporal provenance table records product-file identities, nominal observation periods, known release information and unknown encoder-training cutoffs. Last-modified timestamps identify the retrieved objects; they do not date the first public release.

Temporal eligibility is always defined relative to the current target. A 2021 embedding at the location of a 2013 landslide is an admissible pre-target observation for a 2022 event. Auxiliary factors follow the same rule. WorldCover 2021 [23] enters the 2022 and 2024 retrospective tests; in ancillary static comparisons for the 2018–2019 events it cannot be read as pre-event information. The principal embedding-only contrasts do not use land cover.

Events, inventories and satellite inputs

The primary collection has seven earthquake and eleven rainfall events from 2018–2024, with 61,402 landslide locations and 117,059 controls (Table 1). Five events use manually mapped polygons and four use manually labelled GDCLD rasters [24]. Eight rainfall events use satellite-mapped COOLR points [25,26], and Helene uses rapid-response points [27]. Two auxiliary events with model-generated labels are excluded

from primary pooling. RER2023 spans two May storms, and the Mangkhut inventory contains some changes that precede the typhoon reference date.

Polygon and raster inventories contribute one point per object, at its highest cell in the Copernicus GLO-30 DEM [28], as a crown proxy. Point inventories are deduplicated at 30 m. For polygon and raster inventories, controls lie on slopes >5°, 100–2,000 m from mapped failures, within the raster footprint or the polygon-derived hull plus 1 km. COOLR controls are offset 300–3,000 m from event points, lie >200 m from any event-inventory point and pass the same slope filter; these events have no independent survey boundary. The fixed sampling domains support paired comparisons of predictors. Supplementary Text S1 and the event provenance table give inventory sources, coverage and sampling.

Table 1. Events and audit samples. Years denote the available AEF layers. The post-event fraction f is the share of the calendar year after the reference date (365-day approximation).

Event	Trigger	Date	*f*	Inventory (source)	Landslides / controls	Years
Mesetas (Colombia)	earthquake	2019-12-24	0.02	manual raster labels (GDCLD) [24]	1,990 / 3,980	2017–2021
Jishishan (China)	earthquake	2023-12-18	0.04	manual polygons [29]	10,740 / 21,480	2021–2025
Nalgae, Mindanao (Philippines)	rainfall	2022-10-28	0.18	satellite-mapped points (COOLR)	208 / 416	2020–2024
Helene, southern Appalachians (USA)	rainfall	2024-09-27	0.26	rapid-response points [27]	2,213 / 4,426	2022–2025
Palu (Indonesia)	earthquake	2018-09-28	0.26	manual raster labels (GDCLD)	1,522 / 3,044	2017–2020
Mangkhut, Itogon (Philippines)	rainfall	2018-09-15	0.29	manual polygons [30,31]	1,100 / 2,200	2017–2020
Eastern Iburi (Japan)	earthquake	2018-09-06	0.32	manual polygons [32]	5,625 / 11,250	2017–2020
Luding (China)	earthquake	2022-09-05	0.32	manual polygons [33]	8,385 / 16,770	2020–2024
Chittagong (Bangladesh)	rainfall	2023-08-16	0.38	satellite-mapped points (COOLR)	1,764 / 2,921	2021–2025
Northern Vietnam	rainfall	2023-08-04	0.41	satellite-mapped points (COOLR)	1,891 / 3,053	2021–2025
Fujian (China)	rainfall	2023-07-28	0.43	satellite-mapped points (COOLR)	345 / 691	2021–2025
Luzon (Philippines)	rainfall	2023-07-26	0.43	satellite-mapped points (COOLR)	3,133 / 6,422	2021–2025
Lushan (China)	earthquake	2022-06-01	0.58	manual raster labels (GDCLD)	1,286 / 2,572	2020–2024
Agatha (Mexico)	rainfall	2022-05-30	0.59	satellite-mapped points (COOLR)	3,756 / 3,527	2020–2024
Emilia-Romagna (Italy)	rainfall	2023-05-16	0.63	manual polygons [34]	15,000 / 30,000	2021–2025
Freddy (Malawi)	rainfall	2023-03-12	0.81	satellite-mapped points (COOLR)	1,634 / 2,948	2021–2025
Pasaman, West Sumatra (Indonesia)	earthquake	2022-02-25	0.85	manual raster labels (GDCLD)	484 / 968	2020–2024
São Paulo coast (Brazil)	rainfall	2023-02-19	0.86	satellite-mapped points (COOLR)	326 / 391	2021–2025

AEF Satellite Embedding V1 was obtained from the Source Cooperative mirror. Signed 8-bit values v were dequantized as $\text{sign}(v)(v/127.5)^2$, with mask, completeness and vector-norm checks. TESSERA comparisons use identical point sets; seven events have v1 coverage and three use v1.1-cam. Version-specific matched contrasts accompany the ten-event product comparison. Supplementary Data S1–S2 list the source files.

The conventional Sentinel-2 baseline uses nine-channel annual Level-2A reflectance and index composites, with at most one selected scene per tile and month. The controlled-window experiments use a separate all-scene series of red, near-infrared and scene-classification (SCL) bands. Static factors are slope, aspect

sine and cosine, curvature, 330 m relief and elevation. Retrospective models also use log upslope area [35], WorldCover 2021 [23] and, in North Carolina, PRISM precipitation climatology [36].

Paired year substitutions and workflow decomposition

Samples, controls, spatial folds, buffers and model settings are fixed across input years. Spatial k-means defines five folds (ten for Emilia-Romagna), and training locations within 500 m of test locations are removed. The point model is LightGBM [37] with 400 trees, 63 leaves, learning rate 0.05 and row and feature subsampling of 0.8. The patch model uses 11 × 11 cells at 30 m and the CNN2D implementation of Cheng et al. [3]. It is trained with three seeds, Adam optimization (initial learning rate 0.001), batch size 512 and at most 200 epochs. A stratified 15% of each buffered training fold serves for early stopping, which ends training after ten epochs without a validation-loss improvement of 0.0001. Supplementary Text S1 specifies the architecture, normalization, missing-patch handling and all fixed settings. The two models differ in resolution and spatial context as well as in architecture.

For event year Y, the event-year increment is d0 = AUC(Y) − AUC(Y−1). The placebo is AUC(Y−1) − AUC(Y−2), and the year-after increment is d1 = AUC(Y+1) − AUC(Y−1). Subtracting the placebo estimates the excess over the preceding annual drift. Because AEF begins in 2017, the placebo is available for 15 events. The audit changes only the annual information that a model may use; the evaluation design stays the same.

A four-cell training-year × prediction-year comparison separates three components. We write AUC(a→b) for a model trained on year-a inputs and evaluated with year-b inputs. The prediction-only component is then P = AUC(Y−1→Y) − AUC(Y−1→Y−1), the training-only component is T = AUC(Y→Y−1) − AUC(Y−1→Y−1), and the interaction is I = d0 − P − T. The decomposition identifies the workflow in which the input-time effect appears. Cross-event exposure models fit d0 and d1 jointly and account for their shared baseline and for the recovery of the year-after reference. Supplementary Text S5 reports the ratio fits and their uncertainty.

Controlled optical observations and seasonal reference

The optical experiments use one representative interior point from each of 1,100 inventory polygons, together with 2,200 controls, at Eastern Iburi and at Mangkhut. Iburi polygons were sampled with seed 0, and all 1,100 Mangkhut polygons were used. These interior points differ from the crown proxies of the annual audit. Object identities and coordinates were recovered from the source inventories and checked, so no landslide object contributes more than one optical sample.

Ninety-day windows end at −30, −1, +7, +30 or +60 days relative to the event. Sentinel-2 L2A digital numbers are converted with their scale and with the harmonization state of the stored data. Assets already marked as offset-corrected are not corrected a second time, and early zero-offset assets keep a zero offset. Harmonized scenes from both optical cases were checked against the corresponding Collection 1 pixels, and the original metadata, effective offsets and reference values are archived. No scene-level minimum share of valid sample points is imposed. The quality mask keeps SCL classes 4–7 (vegetation, non-vegetated land, water and unclassified). A valid date also requires non-nodata red and near-infrared values, finite reflectance and red + nir > 0. Same-day overlaps are reduced to daily medians, and the reference date is excluded. NDVI is clipped to [−1, 1]. Five features are computed after temporal truncation: the median red, nir and NDVI,

and the 10th and 90th NDVI percentiles.

Each point and window contributes exactly three distinct dates per draw. Ten date-sampling seeds (0–9) each produce a separate LightGBM fit and spatial out-of-fold prediction. We average the ten AUCs and their paired contrasts; predictions from different draws are never averaged for this endpoint. The classifier uses the fixed 400-tree configuration described above with model seed 0. Five spatial folds and a 500 m training buffer are fixed across cutoffs and years. An all-date curve and a single three-date draw serve as sensitivity checks.

The 2018 cutoff curves require at least three valid dates in all five windows. The principal seasonal contrast, D = [AUC2018(+60) − AUC2018(−1)] − [AUC2017(+60) − AUC2017(−1)], uses the points with at least three dates in all four endpoint windows. Complete seasonal curves require all ten windows. Every analysis requires at least 100 points per class and 30 buffered training points per class. In each of 1,000 spatial bootstrap replicates (30 clusters), the same ten draw indices are resampled jointly across windows and years, and the mean of their paired AUC differences gives the interval. Space-only intervals and seed-0 results are also reported. The intervals condition on the fitted models. The principal AUC pools out-of-fold scores, whereas the within-fold sensitivity described below compares only positive–negative pairs scored by the same fitted model. Supplementary Text S2 and Tables S6–S9 document the sample flow, absolute and fold-level AUCs, date selections, scene assets and the scene-gate sensitivity.

Retrospective value and explicit landslide history

North Carolina training records are linked to USLI v3 through USGS_ID. We keep records with confidence ≥5, ordered Date_Min and Date_Max, and Date_Max before 1 January 2024, which leaves 2,711 historical landslides. The training domain is their convex hull plus 1 km. Controls are drawn from its 30 m terrain grid on slopes >5° and more than 100 m from these qualified records. They are sampled at a 2:1 ratio within 5 km spatial strata, allocated by candidate area with seed 0. Neither target-event locations nor date-ineligible records define this domain or its avoidance mask. The fixed target is Helene, with 2,025 landslides and 3,685 controls. USLI v3 was published in February 2025 [38], so this experiment is an occurrence-bounded retrospective test.

Lushan uses 8,833 landslides of the 2013 earthquake and 17,666 controls [39] to predict the June 2022 event, represented by 1,286 landslides and 2,572 controls. The existing spatial split removes the target sample's convex hull plus 1 km from training. The complete 2013 inventory, deduplicated on the original 30 m grid, supplies the history reference. This is a retrospectively defined spatial separation.

Table 2 lists the schemes, which compare conventional factors, prior-year embeddings and explicit history. The historical features are log(1 + distance to the nearest source) and log(1 + number of sources within 1 km). A training positive excludes only its own source identity, so independent neighbouring records remain. Training controls and future-event queries use all qualified sources, including those within 30 m. USGS_ID identifies the North Carolina records; for Lushan, source-row IDs and their exact 10 m cell mapping recover the training identities. Distances ≤100 m and >100 m define near-history and far-history strata, and both classes are restricted to the same stratum. These strata describe proximity, not failure recurrence.

All schemes use 500 LightGBM trees, 63 leaves, learning rate 0.05, row and feature subsampling of 0.8 and seed 0, without tuning on the test set. Inputs are limited to pre-target factors and embeddings, and event-year embeddings are substituted only in the B2 diagnostic prediction. The earlier controls and the uniform

30 m historical exclusion are kept as separate sensitivity designs (Supplementary Text S3). Because the history reference and the training positives overlap, the leave-one-record history of a training point measures clustering within the history. The history of a test point measures how close a later event lies to earlier failures. The two relations need not transfer equally, especially for the single 2013 Lushan event.

Table 2. Retrospective schemes. Conventional factors comprise the available terrain, land-cover, hydrology and climate variables; rock type and roads are not included. Historical records are qualified against the current target.

Scheme	Inputs	Comparison addressed
B0	Conventional factors	Reference discrimination
H	Historical distance and count	Historical spatial signal alone
B1	B0 + historical distance and count	Added value of explicit history
B2	Prior-year AEF	Pre-target embedding value
B3	B1 + prior-year AEF	Embedding increment beyond factors and history
B0+AEF	B0 + prior-year AEF	Fusion without explicit history
Post-event diagnostic	Fixed B2 model, event-year AEF at prediction	Response to post-target input

Map domains and area-based evaluation

Nine events have 30 m spatial out-of-fold maps. Their domains comprise mapped footprints or polygon-derived hulls, slopes >5°, locations within 2 km of the target inventory, and valid AEF inputs in all compared years. We call them target-conditioned domains. The map endpoint is the fraction of mapped landslide area captured within the highest-scoring 5%, 10% or 20% of the evaluated area. Training crown proxies and mapped landslide areas thus provide complementary point and area evaluations.

A second map design covers the full administrative area of Brisighella and Modigliana, with the inventory of Ferrario and Livio [40,41]. It averages five spatial out-of-fold designs over 329,953 cells at 30 m (about 297 km²), all of which have saved predictions in the compared years. This domain does not depend on the proximity of target landslides and is evaluated on the common annual-product support. The two municipalities form one event-level test.

Binary ROC-AUC compares mapped landslide cells with the disjoint remainder of the domain. Top-area capture allocates exactly the specified area budget and shares tied scores proportionally. Average precision uses the same labelled domain. Spatial-cluster intervals use 4,000 score bins; exact point estimates and the approximation errors are archived. Supplementary Text S4 gives the score-bin approximation and the paired uncertainty calculation.

Statistical inference and reproducibility

The primary audit endpoints are the paired AUC difference and the paired difference in top-10% capture. A paired spatial-cluster bootstrap with 1,000 resamples shares the sampled clusters across all comparisons. The principal AUC ranks pooled out-of-fold scores. A sensitivity analysis weights each fold AUC by its positive count times its negative count, so that it compares only within-fold pairs. The pair weights are recalculated in every bootstrap replicate, and optical date draws remain paired across the four endpoints. Equal-fold means are reported as point estimates. The two AUC definitions compare different sets of sample pairs, so they can

differ with geographic composition and with score scales across fold models; no folds or samples change.

Event-level means use the DerSimonian–Laird estimator [42]. REML with Hartung–Knapp–Sidik–Jonkman intervals provides a robustness analysis and the between-event heterogeneity [43–45]. Approximate prediction intervals combine heterogeneity and the uncertainty of the mean with a t reference on k − 2 degrees of freedom. We also omit one event or one country group at a time. Equivalence tests use margins of ±0.01 for point AUC and ±0.02 for map capture [46,47]. Other capture fractions, products, history strata and exposure fits are secondary analyses. Bootstrap intervals condition on the fitted models and on the sampled inventory. Local protocols and execution hashes record the order of the analyses; they are not a public preregistration. Scripts, paired predictions, provenance tables and a small worked example support reconstruction of the figures and quantitative results.

Results

Inflation persists across events and pre-event drift controls

With prior-year AEF, the median within-event AUC was 0.81 for the point model and 0.80 for the patch model. Under the principal pooled out-of-fold metric, event-year inputs increased AUC in all 18 point-model events and in 16 of 18 patch-model events (Fig. 2). The mean increments were 0.0874 (95% confidence interval 0.0649–0.1098) and 0.0705 (0.0475–0.0934). Subtracting the preceding annual drift left 0.085 (0.057–0.113) and 0.064 (0.035–0.093) across 15 events. Both primary AEF placebos were equivalent to zero within the specified margins.

The average effect did not depend on any single event or country group. Leaving one out gave point effects of 0.080–0.094 and patch effects of 0.062–0.077. REML estimates were close to the primary means, with between-event standard deviations of 0.050 and 0.053 AUC. Event effects ranged from small to large, and the approximate prediction intervals for a new event were −0.022 to 0.197 for the point model and −0.044 to 0.186 for the patch model. The data show a stable average inflation with substantial variation between events.

Two further checks address different questions. The first changes the AUC definition in all 18 events. When only within-fold positive–negative pairs were compared, the mean increments under the same random-effects estimator were 0.082 (0.062–0.103) for the point model and 0.069 (0.050–0.088) for the patch model. Point-model increments stayed positive in 17 of 18 events; Jishishan changed from +0.026 to −0.010 (Table S19). The second check concerns preprocessing in a single event. Mangkhut had the highest fraction of missing patch cells. There, estimating the imputation means only from the inner fitting subset changed the annual CNN increment from 0.1073 to 0.1096, a paired change of +0.0024 (+0.0003 to +0.0045) (Table S21). This check was not repeated in the other 17 events, so the 18-event patch mean has not been recomputed under the stricter imputation.

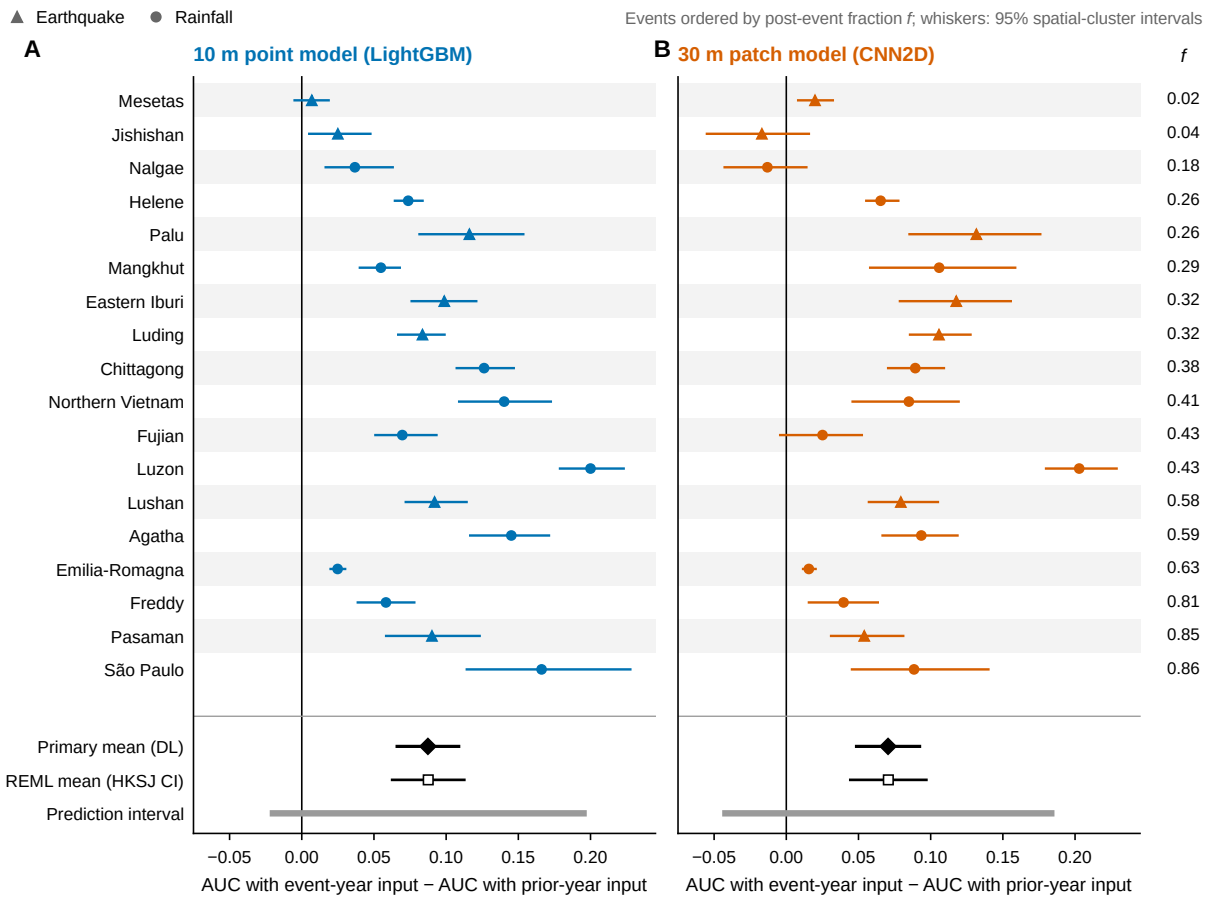


Fig. 2. Event-year AEF increments under fixed spatial validation. Each row is one event, ordered by the post-event fraction f (right-hand column); triangles mark earthquakes and circles rainfall events. Markers and whiskers show the paired AUC difference between event-year and prior-year inputs with its 95% spatial-cluster bootstrap interval, for (A) the 10 m point model and (B) the 30 m patch model. Below the events: the primary DerSimonian–Laird (DL) mean, the REML mean with its Hartung–Knapp–Sidik–Jonkman (HKSJ) interval, and the approximate REML prediction interval for a new event.

Apparent skill rises at a fixed observation count

At Iburi, the five-cutoff support contains 474 landslide objects and 1,008 controls. The mean three-date AUC rose from 0.453 at −1 day to 0.791 at +60 days, an increment of +0.337 (+0.289 to +0.380). With all valid dates, the increment was +0.391 (+0.325 to +0.450). The separate four-endpoint support has 281 landslides and 972 controls. On it, the 2018 change was +0.390 and the 2017 change −0.032, so the excess over the preceding season was +0.423 (+0.353 to +0.479).

At Mangkhut, the five-cutoff support contains 1,080 landslide objects and 2,089 controls. The mean three-date AUC rose from 0.472 to 0.766, an increment of +0.293 (+0.258 to +0.329). The all-date increment was +0.345 (+0.305 to +0.390). On the four-endpoint support (315 landslides and 442 controls), the 2018 change was +0.311 and the 2017 change +0.080, an excess of +0.231 (+0.164 to +0.293).

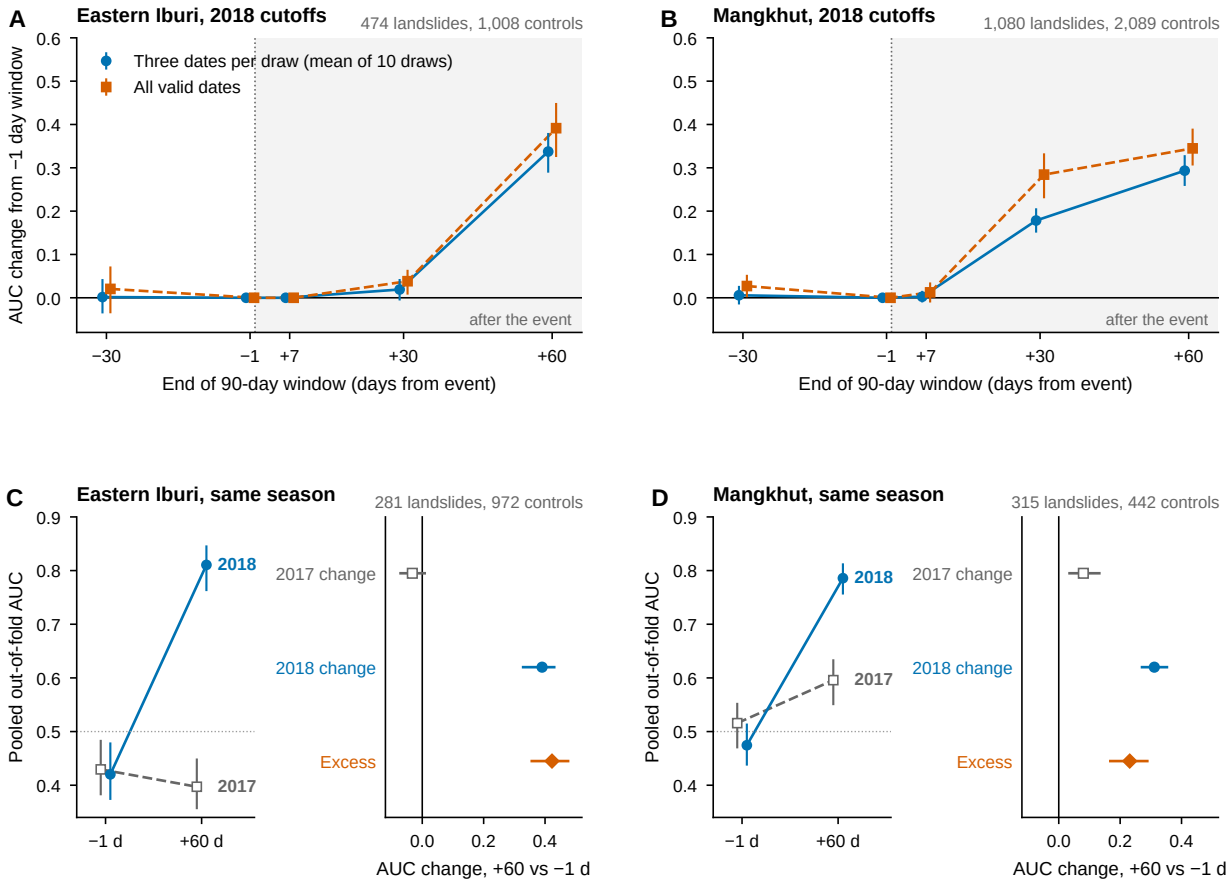


Fig. 3. Controlled optical observation timing after asset-level scaling. (A, B) AUC change relative to the window that ends 1 day before the event, for 90-day windows ending at five offsets, on each event's five-window support (the shaded area lies after the event). Circles average ten separately evaluated three-date draws; squares use all valid dates. (C, D) Four-endpoint common support. Left: pooled out-of-fold AUC at −1 and +60 days in the event year (2018) and the preceding year (2017); the dotted line marks AUC = 0.5. Right: the +60 minus −1 day change in each year and their difference (excess over 2017). Intervals combine paired spatial-cluster and date-draw resampling. Absolute pooled AUCs are listed in Table S7, and within-fold levels and contrasts in Table S20.

The within-fold pair-weighted sensitivity also gave positive seasonal excesses, 0.335 (0.255–0.402) at Iburi and 0.191 (0.117–0.260) at Mangkhut. Under this metric the 2018 −1-day AUC at Iburi is 0.551, against 0.420 for pooled out-of-fold scores. Absolute pre-event levels and effect sizes depend on which spatial sample pairs are compared, whereas the excess over the seasonal reference stays positive (Table S20).

The fixed-count endpoint describes the expected discrimination of a three-date draw. Single-draw results, absolute four-endpoint AUCs and an audit of date unions make this information budget explicit. The complete ten-window seasonal support and the scene-gate check are reported with the principal comparisons, including the analyses that did not reach the sample threshold. These results concern separability on the stated optical supports, and Mangkhut retains its mixed inventory dates.

Workflow and product choice determine the size of the effect

The training-year × prediction-year experiment places most of the inflation in the matched use of event-year inputs for training and testing (Fig. 4A). Changing only the prediction inputs gave a pooled point effect of 0.0006 (−0.011 to 0.013), with event-specific effects from −0.068 to 0.052; the patch mean was −0.011

(−0.027 to 0.006). Training on event-year inputs and testing on pre-event inputs reduced AUC by 0.043 (point) and 0.053 (patch). The interaction was positive in every event. It exceeds the joint year-swap increment because it offsets this training-only loss. Event-related surface information is therefore most useful when both sides of the spatial evaluation share the same temporal state.

The pattern holds across representations. On ten matched point sets, the TESSERA increment was 0.104 (0.073–0.135), against 0.071 (0.047–0.094) for AEF. In the seven-event TESSERA v1 subset, the paired excess over AEF was 0.022 (HKSJ interval about 0.000–0.043); the three-event v1.1-cam subset is reported separately (Fig. 4B). The TESSERA placebo was not equivalent to zero within ±0.01. We rebuilt the annual Sentinel-2 point composites from cached digital numbers, with asset scaling that accounts for harmonization. They gave a mean increment of 0.121 (0.052–0.190) across 15 events, with increases and decreases among single events (Table S5). For assets whose harmonization the independent pixel check could not resolve, treating the remaining offset as already applied gave a sensitivity mean of 0.128 (0.057–0.200).

Single events are sensitive to this unresolved scaling even though the positive average remains. Nalgae changed from −0.061 to +0.004 (paired change +0.065, −0.058 to +0.203), and Chittagong and Emilia-Romagna changed by +0.028 and +0.022 (Table S5). Five of Nalgae's 12 event-year scenes remain unresolved; they account for 35.7% of the valid scene-point observations on its audit support. The products also differ in their pre-event baselines, which matters when increment magnitudes are compared. What they share is a dependence on the time that the inputs represent, in learned embeddings and in conventional composites alike.

Cross-event exposure fits relate the increment to the fraction of the calendar year after the event. The relation persists in recovery-adjusted AEF fits, with half-saturation point estimates around 0.23–0.26. Several fits are uncertain, and Mangkhut departs from the common response. The fitted curves describe variation among these products and events (Supplementary Text S5, Table S14 and the archived fit tables).

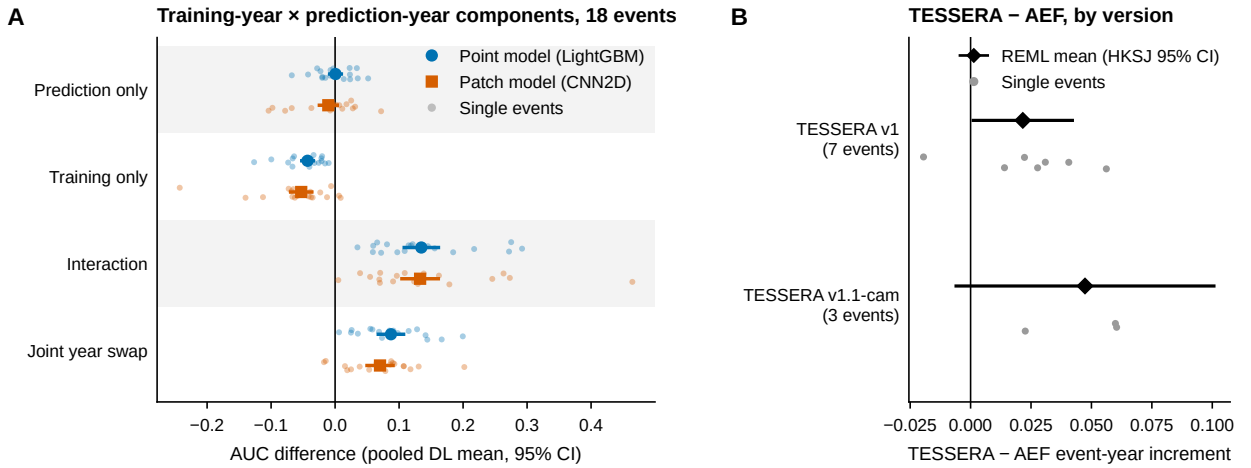


Fig. 4. Workflow and version dependence. (A) Prediction-only, training-only, interaction and joint year-swap components across 18 events, pooled with the primary DL estimator (large markers, 95% CI); faint dots are single events. Components add at event level, but separately pooled summaries use different weights. (B) Paired TESSERA-minus-AEF increments within each TESSERA version subset: REML means with HKSJ 95% intervals (diamonds) and single events (dots). The version groups comprise different events.

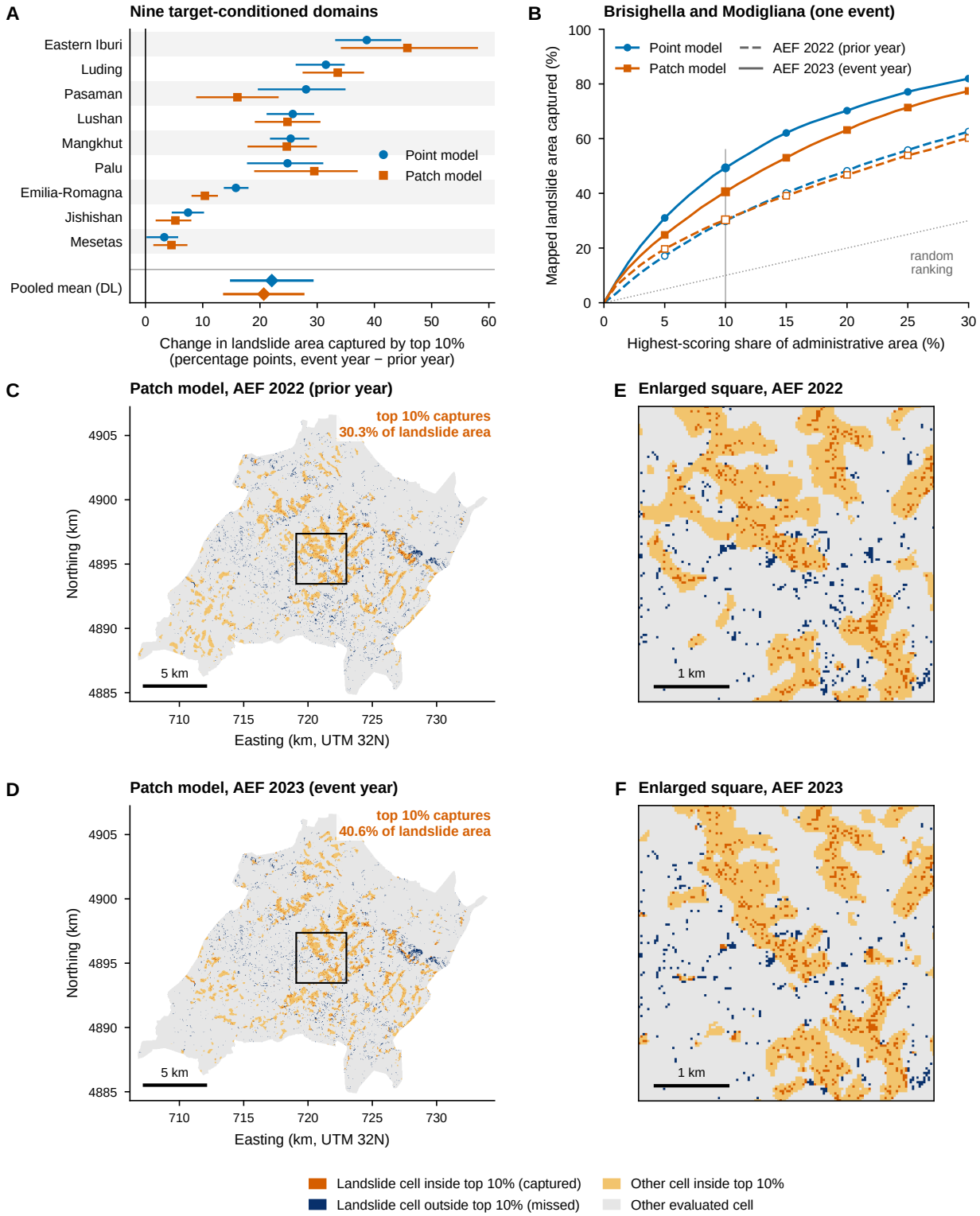


Fig. 5. Map consequences of input-year choice. (A) Change in top-10% landslide-area capture (event-year minus prior-year input) in nine target-conditioned domains, with the pooled DL means. (B) Capture curves across Brisighella and Modigliana, Emilia-Romagna, Italy; markers show capture at 10% of the area, and the dotted line is the expectation under random ranking. (C, D) Outcome of the patch-model top decile with prior-year (2022) and event-year (2023) inputs over the full administrative grid (WGS84/UTM 32N, EPSG:32632): landslide cells inside the top decile (captured) and outside it (missed), and other top-decile cells. (E, F) The approximately 3.9 km square outlined in C and D, centred on the domain's median row and column. Scores average five spatial out-of-fold designs; the 329,953 cells at 30 m represent one event.

Input timing changes which areas rank highly

The effect carries over from point discrimination to the spatial concentration of mapped failures (Fig. 5). Across the nine target-conditioned domains, top-10% capture increased by 22.1 percentage points for the point model (14.8–29.4) and by 20.7 points for the patch model (13.6–27.8). Capture increased in all nine events, and the smallest changes were comparable to the variation of the map placebo. These numbers are changes in the share of landslide area captured within the same area budget, not changes in overall accuracy.

The administrative-domain maps show the same direction without a target-proximity restriction. Across Brisighella and Modigliana, point-model top-10% capture rose from 0.300 to 0.493, a gain of 19.3 percentage points (14.3–25.4). Patch-model capture rose from 0.303 to 0.406, a gain of 10.3 points (5.1–15.4). Exact average precision rose from 0.074 to 0.150 and from 0.088 to 0.123, at a mapped landslide prevalence of 3.04%. The choice of the event-year layer thus changes both the apparent discrimination and the share of mapped damage that falls in the highest-ranked area.

Pre-event value depends on the historical baseline

In North Carolina, conventional factors reached an AUC of 0.726, history alone 0.585 and prior-year AEF alone 0.774 (Fig. 6A). Adding history to the factors gave 0.697, a paired change of −0.030 (−0.065 to +0.001). Adding AEF to this historical baseline gave 0.756, a further +0.059 (+0.044 to +0.077). Factors plus AEF reached 0.777, which is +0.051 (+0.033 to +0.067) above factors alone.

In Lushan, conventional factors reached 0.568, history alone 0.724 and prior-year AEF alone 0.594 (Fig. 6B). Adding history to the factors gave 0.728, a paired change of +0.160 (+0.070 to +0.238). Adding AEF to this baseline gave 0.736, a further +0.008 (−0.007 to +0.022). Factors plus AEF reached 0.600, or +0.032 (−0.026 to +0.081) above factors alone.

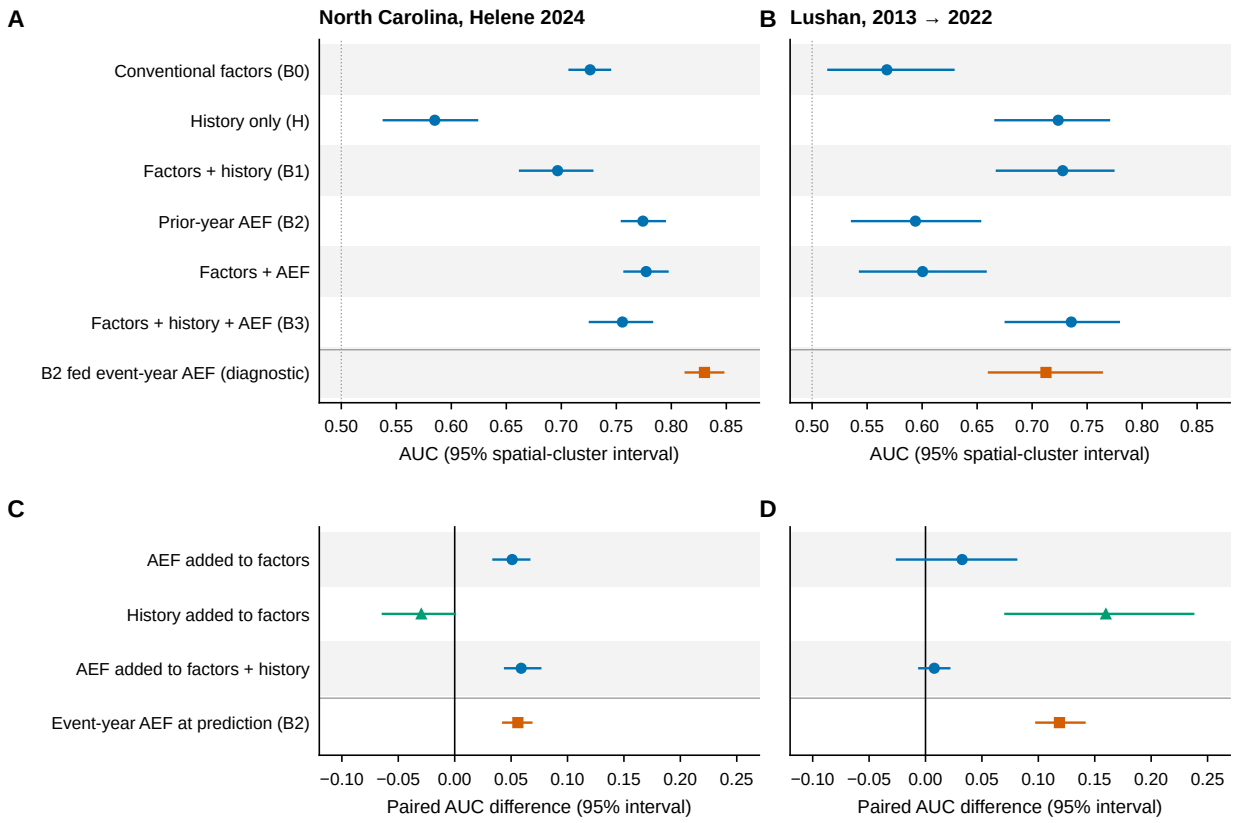


Fig. 6. Retrospective value of pre-target inputs. (A, B) AUC of the six pre-target schemes and of the separately marked B2 post-event diagnostic. (C, D) Paired increments against their stated baselines. North Carolina uses 2,711 occurrence-qualified historical records and 5,422 controls generated from those records alone; Lushan uses the 2013 inventory for the 2022 target. Intervals are paired spatial-cluster intervals conditional on the fitted models.

Explicit history changes the baseline against which an embedding increment is judged. Identity-aware history and the earlier 30 m exclusion gave similarly small additional embedding increments in Lushan. The sensitivity tables show how the construction of historical features and the North Carolina control sampling affect all schemes. The history-only model also shows whether a weak fusion result reflects a lack of historical spatial signal or a difficulty in transferring the fitted relation.

With the B2 model fixed, substituting event-year AEF at prediction changed AUC by +0.056 (+0.042 to +0.069) in North Carolina and by +0.119 (+0.097 to +0.142) in Lushan. These diagnostics measure the effect of the prediction input within B2. The B3 − B1 contrasts answer a different question: the value of adding pre-target embeddings to factors and history. Table S11 gives distance-stratified counts and intervals; strata with fewer than 30 observations in either class are not estimated.

Table 3. Principal effects and evidence units. AUC changes are absolute; capture changes are percentage points. Detailed intervals and sensitivity results accompany the figures and the Supplementary Materials.

Evidence	Main finding	Unit of interpretation
Annual AEF audit	Point +0.0874; patch +0.0705 AUC	18 events under fixed spatial validation
Prior annual drift control	Point +0.085; patch +0.064 AUC	15 events with Y−2
Map concentration	Point +22.1; patch +20.7 percentage points	Nine target-conditioned map domains
Administrative maps	Point +19.3; patch +10.3 percentage points	Two municipalities, one event
Controlled optical inputs	Iburi +0.337; Mangkhut +0.293 AUC	Three dates per draw, +60 versus −1 day
Pre-target AEF beyond factors and history	North Carolina +0.059; Lushan +0.008 AUC	Two retrospective regional tasks

Discussion

Predictor timing as a validation variable

Annual satellite embeddings describe the land surface well. The same descriptive power can make the aftermath of an event useful to a susceptibility model that is evaluated on that event. In this collection, changing the allowed input year raised AUC by about 0.07–0.09 and moved a substantial share of landslide area into the top-ranked tenth of a map. Pre-event drift correction and the omission of single events or country groups left the average effect in place. Evaluations of annual representations should therefore treat predictor timing as explicitly as spatial separation and label chronology.

The problem lies in the relation between a product and the target it is used to predict. Post-event imagery is valuable for mapping landslides and other disturbances [48,49], and past failures can inform susceptibility to future events. Leakage arises when evidence of the target's consequences enters an assessment of anticipatory skill. The issue concerns the availability of information, whether the representation is a conventional composite or a foundation-model embedding.

From observation timing to workflow-dependent gains

The optical experiments show that moving the observation cutoff past the event changes discrimination even when the number of valid input days is fixed. The year-substitution and workflow experiments extend this result to released annual products: event-year training and testing share information that transfers poorly back to the pre-event surface. Together these results point to post-event surface change as an important source of the apparent gain. Landslide scars, canopy removal and exposed ground are plausible contributors. The independent Emilia-Romagna disturbance diagnostic also found higher event-year AEF scores for riverbank and field damage. When a landslide-trained model was applied to those sites, the disturbance-versus-undisturbed AUC rose from 0.70 to 0.75 (Supplementary Text S5), so the shared signal can include broader surface disturbance.

The preceding-year reference measures seasonal change at the same locations with the same observation count. Comparing the event year with it estimates the excess separability relative to that seasonal reference. Evaluating each three-date draw separately prevents prediction averaging from turning a nominal three-date input into a wider date ensemble. Absolute AUCs under both aggregation rules separate the pre-event level from the later gain; the pooled Iburi value below 0.5 does not appear in the within-fold comparison. Weather and recovery can still differ between years. Because precomputed AEF vectors aggregate several sensor

streams, the optical contrast is a controlled input test, not a measurement of the encoder's internal weighting.

Exposure–response fits describe when annual aggregation has had time to include post-event information. The empirical half-saturation estimates summarize these events only. The year-after signal decays by roughly a quarter per year (recovery ratios 0.770 and 0.762; Supplementary Text S5), which is consistent with the gradual revegetation of landslide scars [50]. Cloud availability, product construction and recovery all vary, so a universal calendar threshold would be inappropriate. For a given application, the actual availability of observations is more informative than the day of year of the event.

Temporal audits change the evaluation of practical value

The map results make the size of the effect concrete. A gain of about 21 percentage points means that an additional fifth of the mapped landslide area falls in the highest-scoring tenth of the evaluated region. Where susceptibility maps support zoning for land-use planning [12], such a shift changes which areas are flagged. The administrative-domain check shows that the direction holds without the target-proximity restriction in one event. Temporal eligibility can therefore change how successful a susceptibility map appears at a fixed area budget.

The retrospective tests keep a positive question in view: what useful information exists before the target? In North Carolina, conventional factors plus pre-target AEF gave the highest tested pre-target discrimination. In Lushan, explicit historical instability supplied most of the improvement and left a small additional embedding effect. Historical information has practical value in its own right [51,52], and representing it explicitly shows whether embeddings add to that information or largely overlap with it. Fang et al. [4] likewise used previous-year embeddings in Taiwan. Regional differences can reflect sampling, trigger conditions and prior instability, so an informative baseline says more than the headline AUC of a product.

For applications, the audit has three linked steps: specify the target and the observation cutoff; compare representations under a fixed spatial and temporal design; and report their incremental value against conventional and historical information in an explicit map domain. Reconstructing a historically deployable forecast additionally requires product release, encoder-training information and record confirmation. The provenance fields and paired outputs released with this study make these choices inspectable and reproducible.

Scope and transfer

The evidence spans several products, two model contexts and 18 heterogeneous events. Landslide inventories differ in type, completeness and mapping method [53]. Here they combine manual polygons, labelled rasters and point records, and the point inventories have no independent survey footprints. Some evaluation domains also depend on target locations. Mangkhut contains mixed occurrence dates; excluding points within 500 m or 1 km of mapped mining areas [54] left its event-year increments positive (Table S17). North Carolina training controls now depend only on occurrence-qualified history, but confirmation dates for the released inventory are not established. Lushan keeps a spatial split based on the target region. The retrospective comparisons apply to these explicitly defined tasks.

The optical seasonal comparisons retain 25.5% and 28.6% of the initial Iburi and Mangkhut landslide objects, and their common support differs in terrain. The median slope of retained Iburi landslides is 18.7°, against 22.3° for excluded ones, whereas Mangkhut landslide slopes are similar (31.6° and 31.7°). Controls shift

toward gentler slopes at both events (Table S22). At Mangkhut, WorldCover 2021 classifies 74.6% of the retained and 51.8% of the excluded landslide samples as tree cover (Iburi: 66.2% and 71.3%). This layer describes the surface three years after the 2018 events. It cannot reconstruct the pre-event vegetation, and it does not show whether the optical effect is overestimated or underestimated. The optical estimates describe the observed common support, and the map comparisons use the common annual-product support. These design features are recorded with the results and should be matched when the benchmark is reused.

The average effect is consistent across the controlled comparisons, which supports a general validation concern; the event-level distributions show why its size should be estimated for each new application. Future benchmarks can extend the audit to more regions and disturbance types. Its central requirement stays the same: information that records the target's consequences must be kept apart from information used to anticipate it.

Conclusions

Annual satellite embeddings can turn post-event surface information into apparent landslide susceptibility skill under spatial cross-validation. Across 18 events, event-year AEF raised AUC by 0.0874 for a point model and 0.0705 for a patch model, with little reduction after pre-event drift correction. The positive average effect extends to TESSERA and to corrected annual optical point composites, and it changes top-10% map capture by about 21–22 percentage points. Controlled optical inputs and workflow comparisons link these gains to observation timing and to event-year information shared between training and testing. Pre-event representations retain regional predictive value, and their added contribution becomes clearer when historical instability is represented explicitly. Temporal auditing is needed both for credible benchmarking of annual Earth-observation representations and for deciding how to use them in event prediction.

Acknowledgments

Funding: This research did not receive any specific grant from funding agencies in the public, commercial or not-for-profit sectors.

Author contributions: Yifan Du: Conceptualization, Methodology, Software, Investigation, Formal analysis, Resources, Visualization, Supervision, Project administration, Writing – original draft, Writing – review & editing. Tianhe Zheng: Investigation. Peiyan Yang: Investigation. Yibo Li: Data curation, Resources. Junhang Zhou: Validation, Formal analysis, Visualization. Kun Yang: Writing – original draft, Writing – review & editing.

Competing interests: The authors declare that they have no competing interests.

Data Availability

Code, the analysis log, per-sample predictions, provenance tables and derived data are archived at Zenodo [55] (version 2.0; https://doi.org/10.5281/zenodo.23467611 resolves to the latest version). The archive provides versioned code and environment specifications, per-sample annual and optical predictions, optical date selections and asset metadata, historical-reference and control-sampling records, figure and table inputs, and executable verification and reconstruction entry points. Compact feature matrices allow the revised retrospective and annual optical models to be refitted without downloading satellite imagery. The archive also contains within-fold statistics, sampled land-cover blocks, per-array missingness records and the two

Mangkhut patch arrays used for the targeted CNN check. Replay entry points bind cached predictions to hashes of the inputs, spatial design, parameters and code. Source-specific acquisition and licence information is included. Version 1.0 of the archive (https://doi.org/10.5281/zenodo.23467612) accompanies an earlier preprint of this work (https://doi.org/10.31223/X5RB93). The AlphaEarth Foundations Satellite Embedding dataset is produced by Google and Google DeepMind.

Supplementary Materials

Supplementary Text S1 to S5, Tables S1 to S22 and Fig. S1 are provided in a separate file. Supplementary Data S1 and S2 list the AlphaEarth and TESSERA source files.

References

1. Brown CF, Kazmierski MR, Pasquarella VJ, Rucklidge WJ, Samsikova M, Zhang C, et al. AlphaEarth Foundations: An embedding field model for accurate and efficient global mapping from sparse label data. arXiv. 2025. https://doi.org/10.48550/arXiv.2507.22291
2. Feng Z, Atzberger C, Jaffer S, Knezevic J, Sormunen S, Young R, et al. TESSERA: Temporal embeddings of surface spectra for Earth representation and analysis. arXiv. 2025. https://doi.org/10.48550/arXiv.2506.20380
3. Cheng Y, Zhu Q, Fan L. From landslide conditioning factors to satellite embeddings: Evaluating the utilisation of Google AlphaEarth for landslide susceptibility mapping using deep learning. arXiv. 2026 (v2). https://doi.org/10.48550/arXiv.2601.07268
4. Fang J, Luo W, Huang Q, Li W, Chen Y-C, Liu C-C. Annual geospatial foundation model embeddings for landslide susceptibility assessment in Taiwan. npj Nat Hazards. 2026 (article in press, published online 16 September 2026). https://doi.org/10.1038/s44304-026-00268-7
5. Li M, Li W, Liu H, Liang C. Leveraging geospatial foundation model embeddings for local-scale landslide susceptibility mapping via positive-unlabeled learning. Research Square. 2026. https://doi.org/10.21203/rs.3.rs-10786241/v1
6. Liu W, Li S, Shi C, Zhu H, Huang C, Yin L. Landslide mapping and susceptibility assessment in the middle and lower reaches of the Nujiang River (2017–2025) using satellite embedding and multidimensional environmental factors. Remote Sens. 2026;18:1854. https://doi.org/10.3390/rs18111854
7. Knezevic J, Atzberger C, Feng Z, Pellegrini AFA, Keshav S, Coomes D. Annual Earth-observation embeddings encode wildfire disturbance and support simplified burned area mapping. arXiv. 2026. https://doi.org/10.48550/arXiv.2609.25731
8. Thasma S, Ho Y-H, Mostafavi A. Beyond backscatter: AlphaEarth land-cover priors for rapid SAR flood segmentation across foundation backbones. arXiv. 2026. https://doi.org/10.48550/arXiv.2606.29134
9. Zhuang Y, Hobeichi S, Shi P, Huang F. Evaluating AlphaEarth Foundations embeddings for wildfire susceptibility mapping. arXiv. 2026. https://doi.org/10.48550/arXiv.2608.12663
10. Reichenbach P, Rossi M, Malamud BD, Mihir M, Guzzetti F. A review of statistically-based landslide susceptibility models. Earth-Sci Rev. 2018;180:60–91. https://doi.org/10.1016/j.earscirev.2018.03.001
11. Merghadi A, Yunus AP, Dou J, Whiteley J, ThaiPham B, Bui DT, et al. Machine learning methods for landslide susceptibility studies: A comparative overview of algorithm performance. Earth-Sci

Rev. 2020;207:103225. https://doi.org/10.1016/j.earscirev.2020.103225

12. Fell R, Corominas J, Bonnard C, Cascini L, Leroi E, Savage WZ. Guidelines for landslide susceptibility, hazard and risk zoning for land use planning. Eng Geol. 2008;102:85–98. https://doi.org/10.1016/j.enggeo.2008.03.022
13. Brenning A. Spatial prediction models for landslide hazards: review, comparison and evaluation. Nat Hazards Earth Syst Sci. 2005;5:853–862. https://doi.org/10.5194/nhess-5-853-2005
14. Roberts DR, Bahn V, Ciuti S, Boyce MS, Elith J, et al. Cross-validation strategies for data with temporal, spatial, hierarchical, or phylogenetic structure. Ecography. 2017;40:913–929. https://doi.org/10.1111/ecog.02881
15. Ploton P, Mortier F, Réjou-Méchain M, Barbier N, Picard N, et al. Spatial validation reveals poor predictive performance of large-scale ecological mapping models. Nat Commun. 2020;11:4540. https://doi.org/10.1038/s41467-020-18321-y
16. Karasiak N, Dejoux J-F, Monteil C, Sheeren D. Spatial dependence between training and test sets: another pitfall of classification accuracy assessment in remote sensing. Mach Learn. 2022;111:2715–2740. https://doi.org/10.1007/s10994-021-05972-1
17. Guzzetti F, Reichenbach P, Ardizzone F, Cardinali M, Galli M. Estimating the quality of landslide susceptibility models. Geomorphology. 2006;81:166–184. https://doi.org/10.1016/j.geomorph.2006.04.007
18. Lombardo L, Tanyas H. Chrono-validation of near-real-time landslide susceptibility models via plug-in statistical simulations. Eng Geol. 2020;278:105818. https://doi.org/10.1016/j.enggeo.2020.105818
19. Kaufman S, Rosset S, Perlich C, Stitelman O. Leakage in data mining: Formulation, detection, and avoidance. ACM Trans Knowl Discov Data. 2012;6:15. https://doi.org/10.1145/2382577.2382579
20. Kapoor S, Narayanan A. Leakage and the reproducibility crisis in machine-learning-based science. Patterns. 2023;4:100804. https://doi.org/10.1016/j.patter.2023.100804
21. Steger S, Schmaltz E, Glade T. The (f)utility to account for pre-failure topography in data-driven landslide susceptibility modelling. Geomorphology. 2020;354:107041. https://doi.org/10.1016/j.geomorph.2020.107041
22. Google DeepMind. AlphaEarth Foundations helps map our planet in unprecedented detail [official release announcement]. 30 July 2025. https://deepmind.google/blog/alphaearth-foundations-helps-map-our-planet-in-unprecedented-detail/
23. Zanaga D, Van De Kerchove R, Daems D, De Keersmaecker W, et al. ESA WorldCover 10 m 2021 v200 [dataset]. Zenodo; 2022. https://doi.org/10.5281/zenodo.7254221
24. Fang C, Fan X, Wang X, Nava L, Zhong H, et al. A globally distributed dataset of coseismic landslide mapping via multi-source high-resolution remote sensing images. Earth Syst Sci Data. 2024;16:4817–4842. https://doi.org/10.5194/essd-16-4817-2024
25. Juang CS, Stanley TA, Kirschbaum DB. Using citizen science to expand the global map of landslides: Introducing the Cooperative Open Online Landslide Repository (COOLR). PLoS One. 2019;14:e0218657. https://doi.org/10.1371/journal.pone.0218657
26. Mancino S, Sblano A, Lovergine FP, Massimi V, Sethi T, et al. Unified Global Landslide Catalogue (UGLC): A single, standardised global-scale landslide dataset. Earth Syst Sci Data Discuss. 2025. https://doi.org/10.5194/essd-2025-482 (dataset: https://doi.org/10.5281/zenodo.18643456)
27. Burgi PM, Toney LD, Collins EA, Murphy CR, Ellison SM, Schmitt RG, Allstadt KE, et al. Preliminary landslide inventory for landslides triggered by Hurricane Helene (September 2024) [dataset]. U.S. Geological Survey data release; 2025. https://doi.org/10.5066/P14CHGKS

28. European Space Agency. Copernicus DEM (GLO-30) [dataset]. 2022. https://doi.org/10.5270/ESA-c5d3d65
29. Jin J, Chen G. The coseismic landslides induced by 2023 Jishishan earthquake [dataset]. Zenodo; 2025. https://doi.org/10.5281/zenodo.15791003
30. Abancó C, Bennett GL, Matthews AJ, Matera MAM, Tan FJ. The role of geomorphology, rainfall and soil moisture in the occurrence of landslides triggered by 2018 Typhoon Mangkhut in the Philippines. Nat Hazards Earth Syst Sci. 2021;21:1531–1550. https://doi.org/10.5194/nhess-21-1531-2021
31. Abancó C, Jones JN. Areas affected by landslides following Typhoon Mangkhut in Itogon, Philippines, September 2018 [dataset]. NERC EDS Environmental Information Data Centre; 2023. https://doi.org/10.5285/32765a61-8510-4dfc-b7c7-58bad12f8497
32. Zhang S, Li R, Wang F, Iio A. Characteristics of landslides triggered by the 2018 Hokkaido Eastern Iburi earthquake, Northern Japan. Landslides. 2019;16:1691–1708. https://doi.org/10.1007/s10346-019-01207-6 (inventory: https://doi.org/10.5281/zenodo.2577300)
33. Liu H, Xu Y, Hu G, Yuan R, Zhao X, Tang J, Lu L, Xu W. Characteristics of earthquake-triggered landslides under high terrain undulation landscapes: a case study of the secondary effects of the 5 September 2022 Ms 6.8 Luding earthquake, SW China. J Geol Soc. 2025;182:jgs2024-253. https://doi.org/10.1144/jgs2024-253 (inventory: https://doi.org/10.6084/m9.figshare.28944505.v1)
34. Pizziolo M, Berti M, Scaroni M, Generali M, Critelli V, Mulas M, et al. RER2023: the landslide inventory dataset of the May 2023 Emilia-Romagna event – Version 1 [dataset]. Zenodo; 2024. https://doi.org/10.5281/zenodo.13742643
35. Bartos M, et al. mdbartos/pysheds, version 0.5 [software]. Zenodo; 2024. https://doi.org/10.5281/zenodo.3822494
36. Daly C, Halbleib M, Smith JI, Gibson WP, Doggett MK, Taylor GH, Curtis J, Pasteris PP. Physiographically sensitive mapping of climatological temperature and precipitation across the conterminous United States. Int J Climatol. 2008;28:2031–2064. https://doi.org/10.1002/joc.1688
37. Ke G, Meng Q, Finley T, Wang T, Chen W, Ma W, Ye Q, Liu T-Y. LightGBM: A highly efficient gradient boosting decision tree. In: Advances in Neural Information Processing Systems 30. 2017. p. 3146–3154.
38. Belair GM, Jones ES, Luna LV, Mirus BB. Landslide inventories across the United States (ver. 3.0, February 2025) [dataset]. U.S. Geological Survey data release; 2025. https://doi.org/10.5066/P14AJF8I
39. Xu C, Xu X, Shyu JBH. Database and spatial distribution of landslides triggered by the Lushan, China Mw 6.6 earthquake of 20 April 2013. Geomorphology. 2015;248:77–92. https://doi.org/10.1016/j.geomorph.2015.07.002 (inventory: https://doi.org/10.5066/F7KS6Q2P)
40. Ferrario MF. Inventory of landslides triggered by heavy rainfall in the Emilia-Romagna region (Italy) in May 2023 [dataset]. Zenodo; 2023. https://doi.org/10.5281/zenodo.8102429
41. Ferrario MF, Livio F. Rapid mapping of landslides induced by heavy rainfall in the Emilia-Romagna (Italy) region in May 2023. Remote Sens. 2024;16:122. https://doi.org/10.3390/rs16010122
42. DerSimonian R, Laird N. Meta-analysis in clinical trials. Control Clin Trials. 1986;7:177–188. https://doi.org/10.1016/0197-2456(86)90046-2
43. Hartung J, Knapp G. A refined method for the meta-analysis of controlled clinical trials with binary outcome. Stat Med. 2001;20:3875–3889. https://doi.org/10.1002/sim.1009
44. Viechtbauer W. Bias and efficiency of meta-analytic variance estimators in the random-effects model. J Educ Behav Stat. 2005;30:261–293. https://doi.org/10.3102/10769986030003261

45. IntHout J, Ioannidis JPA, Borm GF. The Hartung-Knapp-Sidik-Jonkman method for random effects meta-analysis is straightforward and considerably outperforms the standard DerSimonian-Laird method. BMC Med Res Methodol. 2014;14:25. https://doi.org/10.1186/1471-2288-14-25
46. Schuirmann DJ. A comparison of the two one-sided tests procedure and the power approach for assessing the equivalence of average bioavailability. J Pharmacokinet Biopharm. 1987;15:657–680. https://doi.org/10.1007/BF01068419
47. Lakens D. Equivalence tests: A practical primer for t tests, correlations, and meta-analyses. Soc Psychol Personal Sci. 2017;8:355–362. https://doi.org/10.1177/1948550617697177
48. Behling R, Roessner S, Kaufmann H, Kleinschmit B. Automated spatiotemporal landslide mapping over large areas using RapidEye time series data. Remote Sens. 2014;6:8026–8055. https://doi.org/10.3390/rs6098026
49. Scheip CM, Wegmann KW. HazMapper: a global open-source natural hazard mapping application in Google Earth Engine. Nat Hazards Earth Syst Sci. 2021;21:1495–1511. https://doi.org/10.5194/nhess-21-1495-2021
50. Yunus AP, Fan X, Tang X, Jie D, Xu Q, Huang R. Decadal vegetation succession from MODIS reveals the spatio-temporal evolution of post-seismic landsliding after the 2008 Wenchuan earthquake. Remote Sens Environ. 2020;236:111476. https://doi.org/10.1016/j.rse.2019.111476
51. Samia J, Temme A, Bregt A, Wallinga J, Guzzetti F, Ardizzone F, Rossi M. Do landslides follow landslides? Insights in path dependency from a multi-temporal landslide inventory. Landslides. 2017;14:547–558. https://doi.org/10.1007/s10346-016-0739-x
52. Samia J, Temme A, Bregt A, Wallinga J, Guzzetti F, Ardizzone F. Dynamic path-dependent landslide susceptibility modelling. Nat Hazards Earth Syst Sci. 2020;20:271–285. https://doi.org/10.5194/nhess-20-271-2020
53. Guzzetti F, Mondini AC, Cardinali M, Fiorucci F, Santangelo M, Chang K-T. Landslide inventory maps: New tools for an old problem. Earth-Sci Rev. 2012;112:42–66. https://doi.org/10.1016/j.earscirev.2012.02.001
54. Maus V, Giljum S, da Silva DM, Gutschlhofer J, da Rosa RP, Luckeneder S, et al. An update on global mining land use. Sci Data. 2022;9:433. https://doi.org/10.1038/s41597-022-01547-4 (dataset: https://doi.org/10.1594/PANGAEA.942325)
55. Du Y, Zheng T, Yang P, Li Y, Zhou J, Yang K. Code, analysis log and derived data for "Temporal leakage in annual satellite embeddings inflates landslide susceptibility assessments" (version 2.0) [dataset]. Zenodo; 2026. https://doi.org/10.5281/zenodo.23467611

Supplementary material

Temporal leakage in annual satellite embeddings inflates landslide susceptibility assessments

Methods precede the principal numerical results and sensitivity analyses. The companion version history records changes to earlier calculations. Tables S19–S22 quantify AUC aggregation, CNN imputation and optical sample composition; Table S5 includes both annual optical scaling rules. Tables and figure inputs are indexed in `result_index.csv`. Numbers in square brackets refer to the reference list of the main text.

Text S1. Model, sampling and spatial-validation settings

All principal model settings were fixed, without selecting hyperparameters against the target-event test scores. Label 1 denotes a landslide; reported scores are the predicted probability of class 1. Annual input-year comparisons retain the original locations, folds and buffered training masks. New optical comparisons use one point per polygon, so a landslide object cannot cross folds. Controls retain their source sample identity.

For the annual point audit, a 10 m AEF centre vector is used. Spatial KMeans uses 10 folds and 100 bootstrap clusters for Emilia-Romagna and five folds and 30 clusters otherwise (fold seed 0, n_init 5; cluster seed 1, n_init 3). Annual patch eligibility requires valid centre vectors in every compared year and at most 50% cells with a missing channel. The 11 × 11 patches at 30 m aggregate native 10 m cells in 3 × 3 groups. Remaining missing patch values are filled with the channel mean across the retained event-year patches before the spatial split. This label-free imputation uses the retained test-region features in its channel means; normalization thereafter uses only the fitting subset. A scan of all 69 primary event-year arrays records missing values, spatial cells with any missing channel and patches with any missing cell, before and after eligibility. The sensitivity event was selected by the largest retained missing-cell fraction before refitting. Both imputation operators use identical folds, 500 m buffers, inner splits, optimization and three seeds; the stricter operator estimates each channel mean only from the inner fitting subset and applies it to validation and test patches. An absolute change >0.01 in the paired annual increment was the locally specified trigger for considering more events. Table S21 reports the result and the separate archived-model check. The point/patch comparison changes context and resolution as well as architecture.

CNN2D has two 3 × 3 convolution blocks with padding 1: C→2 C and 2 C→4 C channels, each followed by batch normalization, ReLU and 2 × 2 max pooling. Flattened 16 C features enter fully connected layers 16 C→8 C→2 C→2, with ReLU and dropout 0.3 after the first layer. For AEF, C=64. The training-set channel mean and standard deviation (plus 10^{-6}) normalize all subsets. Cross-entropy, Adam, a polynomial learning-rate schedule with power 0.95 over 200 epochs, and early stopping use the settings in Table S1. Each outer fold sets neural seeds to 100 s+k for s=0,1,2 and fold k; predictions are averaged across those three model seeds. The date draws in the optical experiment have a different endpoint: AUC is evaluated before averaging.

Polygon crown proxies are the highest Copernicus GLO-30 DEM cell [28] in each object; raster objects use eight-connected components. Point inventories are deduplicated at 30 m. Polygon controls use the inventory hull plus 1 km; raster controls use the mapping footprint. Both exclude mapped failures and sample slopes >5° at 100–2,000 m from failures. The event provenance table identifies inventories without independent survey footprints. Input validity and spatial-design files in the archive preserve the exact retained audit sample and fold assignment.

For the seven original COOLR events (Agatha, Luzon, northern Vietnam, Chittagong, Freddy, São Paulo and Fujian), exact-date satellite-mapped event records are selected by country and reference date. Exact coordinate duplicates are removed first; a sequential haversine-radius rule then keeps the first point and removes

later neighbours within 30 m. One NumPy default_rng(0) stream is shared across the events in that order. For each event, 3 n background candidates select a positive source uniformly with replacement, a distance uniformly on [300, 3,000] m and a bearing uniformly on [0, 2π). Coordinates use local latitude/longitude distance conversion. Candidates must be >200 m from the original event's positive-point tree; sampled controls subsequently require GLO-30 slope >5° and the retained annual-input support. No fixed final control count is imposed on this seven-event branch. The avoidance tree contains that event's mapped points, not an all-event landslide archive. No additional control-to-control deduplication is implemented.

Nalgae uses the same positive deduplication and distance/bearing distributions in a separate seed-0 run. It generates 6 n candidates, with source selection via pandas sampling with replacement (random_state=0), applies >200 m avoidance, slope >5° and finite elevation, then selects up to 2 n controls without replacement (random_state=0). Raster-derived and polygon controls use the separate 100–2,000 m rule above. The original scripts and fixed point designs are preserved; this audit restores their specification without resampling controls. These distributions are uniform in radial distance, not uniform by annular area.

Table S1

Fixed configurations. Unlisted LightGBM settings use the locked library defaults, including binary objective, 20 minimum observations per leaf, no maximum depth, zero L1/L2 penalties, max_bin 255 and no class weighting. Native missing-value handling is available, but current optical and forward matrices are complete; annual patch handling is described above.

Component	Learner/input	Optimization or sampling	Repetition and uncertainty
Annual point audit	LightGBM, 64 AEF components	400 trees; 63 leaves; learning rate 0.05; row/column fractions 0.8; bagging frequency 1; four threads	Seed equals fold index; fixed spatial folds; 1,000 paired cluster resamples
Annual AEF patch audit	CNN2D, 64 × 11 × 11	Adam; initial lr 0.001; batch 512; ≤200 epochs; validation loss improvement 0.0001; patience 10; stratified validation fraction 0.15 of buffered training	Three seeds per fold; mean class-1 probability; fixed fitted models in bootstrap
Corrected annual S2 point audit	Nine median/index features; LightGBM	Same 400-tree point configuration; original 15-event support and folds; actual asset scaling	Per-event paired annual contrasts; 1,000 cluster resamples
Optical cutoffs	Five red/nir/NDVI summaries; LightGBM	400 trees; 63 leaves; lr 0.05; row/column fractions 0.8; model seed 0	Ten three-date draws, seed 0–9; mean AUC; same 1,000 spatial and draw resamples across windows
Optical spatial design	KMeans on projected point coordinates	Five folds, 30 clusters, n_init 10 and seed 1; 500 m exclusion from test points	≥100 per class per support; ≥30 per class in buffered training
Retrospective schemes	LightGBM, B0/H/B1/B2/B3/B0+AEF	500 trees; other point parameters unchanged; seed 0; no test tuning	NC:100 clusters; Lushan:30; n_init 3, seed 1; 1,000 cluster resamples
NC training controls	30 m grid; qualified-history hull +1 km	Slope>5°; qualified-history distance>100 m; 2:1 controls; 5 km strata by candidate area; largest-remainder quota; seed 0, without replacement	One frozen control sample used by every scheme; no replacement after feature eligibility

Text S2. Optical assets, information budget and sample selection

The observation universe consists of public HTTPS Sentinel-2 L2A COG assets returned by Earth Search for the fixed point bounding boxes and dates. Scene records distinguish points outside a scene, unavailable non-public assets and successful reads. Network failures are not interpreted as missing observations. Pixel quality requires SCL 4,5,6 or 7, non-nodata red/nir and a positive denominator. Class 7 is unclassified, so "valid date" denotes this mask rather than guaranteed clear sky. These choices apply identically to 2017 and 2018. First-valid-date and exposure summaries refer to this asset universe and mask.

Declared scale/offset and harmonization state are reconciled before conversion. The early zero-offset assets use zero; assets marked as already harmonized also use zero effective offset, avoiding a second subtraction. For one actual harmonized scene in each optical case, 16 red and 16 near-infrared pixels match the corresponding Collection 1 values after its documented offset: the reference DN is exactly 1,000 higher. These checks identify the scaling of the stored values, independently of model performance. The asset manifest records collection, scene ID, processing baseline, product identity, scale/offset, nodata, URLs and catalogue hashes. Selected original SAFE tile metadata and tile-info files cross-check scene identity and processing baseline. The pixel-level checks and original/reference DN values are supplied in radiometric_pixel_checks.csv. Annual nonzero-offset assets without a confirmed harmonization flag are additionally compared with Collection 1 or Planetary Computer reference pixels. A resolution requires at least five valid pairs, median reflectance mismatch ≤ 0.01, 90th-percentile mismatch ≤ 0.02, and agreement between red and near infrared. Unresolved cases retain their declared offset in the principal annual point analysis; a separate sensitivity treats that residual offset as already applied. Neither rule is selected by AUC. This sensitivity reports the effect of the remaining ambiguity, without claiming an absolute radiometric validation of every asset. The quality-count table records how many scene-point observations fail denominator checks or have NDVI clipped. Finite negative reflectance alone is not used as proof of an incorrect asset offset.

Daily medians combine overlapping tiles after the validity mask. A window spans 90 calendar dates inclusively; its reference day is omitted. Date selections are sampled without replacement. For a given draw, all five features use that point's same three dates. A classifier is fit separately for every window and draw. The primary statistic is the mean of ten AUCs or paired AUC contrasts, not the AUC of an averaged prediction. The archive retains both quantities for audit, but the ensemble diagnostic does not enter the fixed-count conclusion. Ten draws can cover more than three dates in total; Table S9 and the per-point selections document that union explicitly.

Spatial bootstrap weights are drawn once per support set (seed 1), identically across all windows and years. Within each spatial resample, ten draw indices are sampled with replacement (seed 2) and the mean paired contrast is computed. Percentile intervals come from that final distribution, never from averaged confidence limits. Space-only and single-draw intervals are supplied as sensitivity measures. Scores and model fits remain fixed during this resampling, so full training uncertainty is not included.

All comparisons start from 1,100 polygon objects and 2,200 controls per event. The source-row mapping verifies a maximum of one positive sample per object. Five-cutoff 2018, four-endpoint two-year and ten-window two-year support sets are stored as separate boolean fields, together with their exact intersections. Sequential sample-flow tables name the applied window at each step. Selection summaries report polygon area, local GLO-30 neighbourhood slope, descriptive WorldCover 2021 class and date counts for retained and excluded locations. WorldCover 2021 v200 [23] was sampled from the N42E141 and N15E120 source tiles using WGS84 coordinates, the stored geotransforms and native nearest-pixel indices. All 6,600 candidates have valid class codes. Tile URLs, header hashes, pixel indices and sampled blocks are archived. Land-cover

summaries report class counts and proportions; class-code medians are not used. These slope/land-cover summaries are not model inputs or eligibility criteria; WorldCover 2021 describes the later surface at selected locations, not the pre-event land cover of the 2018 events. Table S22 gives the selection contrasts. Figure S1 shows the spatial distribution. The former 5% scene gate is evaluated using the corrected reflectance on common eligible points.

Text S3. Historical inputs and training-sample construction

North Carolina's qualified reference library is the 2,711 retained USLI v3 records [38]. Each source has a USGS_ID, occurrence interval, qualification decision and snapped 30 m location. The training positives are those records; the new controls use only their domain and avoidance mask. The new 5 km stratum table records candidate counts, allocated quotas and the random seed. Static variables are slope, aspect sine/cosine, curvature, 330 m relief, elevation, log contributing area, WorldCover 2021 and PRISM 1991–2020 precipitation [36]. The DEM hydrology operator matches the earlier training data: pysheds 0.5 [35] pit/depression filling, flat resolution, flow direction and accumulation. Land cover remains numerically encoded as in the original fixed baseline; no target-driven recoding or tuning is introduced.

Lushan uses the 2013 inventory of Xu et al. [39] after 30 m source deduplication. Original source-row identifiers map exactly to the 10 m cells of positive training samples. No nearest-neighbour radius is used to infer self identity. The complete source library remains available to 2022 queries, including sources excluded from training by the target hull+1 km split. Static factors are the North Carolina list without precipitation. Train and test points retain their original terrain processing scales and hydrology fields.

An own-source index is removed from a training positive's nearest-distance search and its 1 km count. Other independent sources remain even inside 30 m. Test points and training controls have no own-source exclusion. The H model uses these two history variables alone. For controlled sensitivity comparisons, the earlier North Carolina controls are used with identity exclusion and then with the previous uniform 30 m exclusion. The latter also excludes test-near history; it is labelled as the previous operator, not as the main history baseline. Lushan has the same two historical operators and unchanged training labels.

The shared test samples allow paired comparisons between designs. Near/far strata use the unmodified nearest-source distance and apply to both classes. A historical training record's leave-one distance describes within-library clustering, whereas a future target's distance describes event-to-history proximity; the two relationships need not transfer equally. Keeping a genuine earlier source near a target is chronologically admissible and is not test-label leakage.

Text S4. Event-level and map-level inference

The event, rather than an individual landslide, is the unit for cross-region pooling. The primary DerSimonian–Laird summary is retained; REML heterogeneity, HKSJ confidence intervals, approximate t-based prediction intervals (k-2 degrees of freedom) and leave-one-event/country summaries are reported. The new-event prediction intervals cross zero for both main AEF models. Detailed omission estimates are in `event_meta.csv`.

The primary AUC compares all positive–negative pairs after pooling out-of-fold scores. The sensitivity AUC is $\Sigma(n_+k\ n_k\ AUCk)/\Sigma(n_+k\ n_k)$, over folds k with both classes. In bootstrap samples, cluster multiplicities determine each fold's positive and negative counts and the weights are recalculated. Folds with zero positive–negative pairs contribute zero weight. Annual sensitivity retains the original 1,000 sampled cluster-index

sequences (seed 1); optical sensitivity uses the existing 30-cluster multinomial sequences (seed 1) with jointly resampled date-draw indices (seed 2). Each optical draw is evaluated before averaging. Equal-fold means are point estimates only. Annual event tables distinguish full-sample point estimates from bootstrap-mean inputs to the original DerSimonian–Laird pooling. Models, folds, sample sets and score direction are unchanged. Tables S19–S20 report both estimands; the paired bootstrap conditions on fitted models.

Mapped positives and negatives are disjoint: positives are inventory cells inside the evaluation domain; negatives are its complement inside that domain. Area capture ranks the whole evaluated domain and allocates exactly 5%, 10% or 20%, sharing the boundary score tie proportionally. Average precision uses this same binary label set. Point estimates are computed from exact scores. The 1,000 spatial-cluster bootstrap uses 4,000 score bins; the archive reports its difference from exact point estimates. Administrative maps use five saved spatial out-of-fold designs averaged before evaluation. Full capture curves, valid support, prevalence and map inputs accompany Table S12. The principal annual map comparison uses common product support, not a reconstructed operational coverage mask.

Text S5. Additional mechanism and exposure evidence

The Emilia-Romagna inventory includes independent river-bank and field-damage polygons. At 2,252 sampled disturbance points, 15,000 landslide crowns and 15,000 undisturbed controls, median AEF change (1-cosine similarity) from 2022 to 2023 was 0.074, 0.048 and 0.042; preceding-year changes were 0.024–0.031. A model trained on landslides versus undisturbed controls scored the disturbance points more highly with event-year inputs: disturbance-versus-undisturbed AUC changed from 0.70 to 0.75, and from 0.71 to 0.79 when restricted to slopes 5–35°. The preceding-year comparison was 0.69→0.70. This supports sensitivity to broader surface disturbance; it does not isolate a uniquely landslide-specific encoder feature.

For the cross-event AEF exposure model, event-year and year-after increments share the prior-year baseline. Their joint 2 × 2 covariance comes from paired spatial bootstrap. The likelihood integrates a normally distributed fully post-event increment using 40-node Gauss–Hermite quadrature and relates the event-year increment to a logistic function of calendar post-event fraction, with positive amplitude, half-saturation in (0, 1) and slope-scale in [0.01, 0.5]. Eight Nelder–Mead starts are refined once; half-saturation intervals are profile-likelihood intervals on 0.02–0.80. Fits reaching boundaries retain those bounds.

AEF year-after-next inputs (17 events) estimate recovery ratios 0.770 (0.661–0.854) for points and 0.762 (0.592–0.898) for patches. Exponential recovery rates are approximately 0.26 and 0.27 per year. Adjusting the year-after reference and its covariance yields half-saturation estimates around 0.23 and 0.26. These describe the current event collection and are not safe-cutoff thresholds. The corrected conventional S2 evidence in this version is the annual point audit and the controlled optical experiments. Earlier S2 patch, fixed 12-month and NDVI-derived mechanism estimates used the superseded offset rule and are retained only in the version history, not as current quantitative evidence.

The four-study literature observation is a targeted search dated 10 October 2026, covering annual-embedding use for dated hazards across arXiv, Research Square, ESS Open Archive and journals, followed by citation checks. Three studies had event-overlapping inputs [3,5,9]; Fang et al. [4] used previous-year inputs with temporal and spatial holdouts. This small, selected literature sample does not estimate field-wide prevalence. Post-event mapping is a distinct legitimate task. A newly mapped annual inventory label is not necessarily a newly occurring failure, but high AUC alone does not diagnose leakage in another study.

Current numerical results

Table S2

Per-event results of the AlphaEarth audit (18 events). n.a.: no Y-2 layer, because AEF begins in 2017. Increments are paired AUC differences with spatial-cluster bootstrap 95% CIs. The increments shown are bootstrap means; the ratio d_0/d_1 is the ratio of the full-sample increments, as used by the joint model in Text S5, and is unstable when d_1 is small.

Event	f	Model	AUC Y-1	Event year (Y - Y-1)	Placebo (Y-1 - Y-2)	Year after (Y+1 - Y-1)	Ratio d0/d1
Mesetas (Colombia)	0.02	LightGBM	0.855	+0.007 (-0.006, +0.019)	+0.022 (+0.009, +0.036)	+0.090 (+0.070, +0.111)	0.07
	0.02	CNN2D	0.878	+0.020 (+0.007, +0.033)	+0.010 (-0.005, +0.026)	+0.081 (+0.066, +0.097)	0.25
Jishishan (China)	0.04	LightGBM	0.591	+0.025 (+0.004, +0.048)	+0.020 (+0.008, +0.032)	+0.026 (+0.003, +0.053)	0.99
	0.04	CNN2D	0.734	-0.017 (-0.056, +0.016)	-0.027 (-0.059, -0.002)	+0.039 (+0.011, +0.070)	-0.44
Nalgae, Mindanao (Philippines)	0.18	LightGBM	0.804	+0.037 (+0.016, +0.064)	+0.012 (-0.009, +0.036)	+0.016 (-0.010, +0.045)	2.13
	0.18	CNN2D	0.768	-0.013 (-0.044, +0.015)	+0.031 (+0.004, +0.061)	-0.026 (-0.055, -0.002)	0.61
Helene, southern Appalachians (USA)	0.26	LightGBM	0.815	+0.074 (+0.064, +0.084)	-0.005 (-0.011, +0.001)	+0.126 (+0.109, +0.146)	0.59
	0.26	CNN2D	0.801	+0.065 (+0.055, +0.078)	-0.010 (-0.020, -0.002)	+0.130 (+0.114, +0.148)	0.50
Palu (Indonesia)	0.26	LightGBM	0.720	+0.116 (+0.081, +0.154)	n.a.	+0.258 (+0.214, +0.298)	0.45
	0.26	CNN2D	0.737	+0.132 (+0.085, +0.177)	n.a.	+0.211 (+0.155, +0.260)	0.63
Mangkhut, Itogon (Philippines)	0.29	LightGBM	0.818	+0.055 (+0.039, +0.069)	n.a.	+0.057 (+0.041, +0.072)	0.97
	0.29	CNN2D	0.763	+0.106 (+0.057, +0.159)	n.a.	+0.070 (+0.035, +0.103)	1.52
Eastern Iburi (Japan)	0.32	LightGBM	0.829	+0.099 (+0.075, +0.122)	n.a.	+0.153 (+0.123, +0.190)	0.65
	0.32	CNN2D	0.830	+0.118 (+0.078, +0.156)	n.a.	+0.153 (+0.112, +0.195)	0.77
Luding (China)	0.32	LightGBM	0.757	+0.084 (+0.066, +0.100)	-0.018 (-0.029, -0.008)	+0.136 (+0.109, +0.163)	0.61
	0.32	CNN2D	0.796	+0.106 (+0.085, +0.128)	-0.012 (-0.031, +0.006)	+0.133 (+0.110, +0.159)	0.80
Chittagong (Bangladesh)	0.38	LightGBM	0.808	+0.126 (+0.106, +0.148)	-0.002 (-0.010, +0.007)	+0.103 (+0.082, +0.126)	1.22
	0.38	CNN2D	0.804	+0.089 (+0.070, +0.110)	-0.004 (-0.015, +0.005)	+0.060 (+0.041, +0.080)	1.49
Northern Vietnam	0.41	LightGBM	0.678	+0.140 (+0.108, +0.173)	+0.013 (-0.004, +0.031)	+0.143 (+0.114, +0.182)	0.98
	0.41	CNN2D	0.721	+0.085 (+0.045, +0.120)	+0.027 (-0.017, +0.071)	+0.074 (+0.035, +0.110)	1.14
Fujian (China)	0.43	LightGBM	0.822	+0.070 (+0.050, +0.094)	-0.008 (-0.026, +0.008)	+0.076 (+0.046, +0.114)	0.92
	0.43	CNN2D	0.800	+0.025 (-0.005, +0.053)	-0.014 (-0.047, +0.020)	+0.016 (-0.016, +0.045)	1.52
Luzon (Philippines)	0.43	LightGBM	0.727	+0.200 (+0.178, +0.224)	+0.007 (-0.002, +0.016)	+0.219 (+0.193, +0.247)	0.91
	0.43	CNN2D	0.729	+0.203 (+0.179, +0.230)	+0.001 (-0.008, +0.012)	+0.210 (+0.184, +0.240)	0.97
Lushan (China)	0.58	LightGBM	0.833	+0.092 (+0.071, +0.115)	+0.003 (-0.007, +0.015)	+0.091 (+0.068, +0.115)	1.01
	0.58	CNN2D	0.842	+0.079 (+0.056, +0.106)	-0.003 (-0.014, +0.006)	+0.081 (+0.057, +0.110)	0.98
Agatha (Mexico)	0.59	LightGBM	0.766	+0.145 (+0.116, +0.172)	-0.010 (-0.024, +0.005)	+0.114 (+0.090, +0.137)	1.27
	0.59	CNN2D	0.789	+0.094 (+0.066, +0.119)	-0.010 (-0.030, +0.010)	+0.055 (+0.031, +0.077)	1.70
Emilia-Romagna (Italy)	0.63	LightGBM	0.908	+0.025 (+0.019, +0.031)	+0.000 (-0.004, +0.005)	+0.024 (+0.017, +0.031)	1.04
	0.63	CNN2D	0.935	+0.016 (+0.011, +0.021)	+0.002 (-0.001, +0.006)	+0.017 (+0.012, +0.023)	0.90

Event	f	Model	AUC Y-1	Event year (Y - Y-1)	Placebo (Y-1 - Y-2)	Year after (Y+1 - Y-1)	Ratio d0/d1
Freddy (Malawi)	0.81	LightGBM	0.853	+0.058 (+0.038, +0.079)	+0.009 (+0.000, +0.019)	+0.044 (+0.020, +0.069)	1.33
	0.81	CNN2D	0.833	+0.040 (+0.015, +0.064)	+0.009 (-0.005, +0.024)	+0.028 (+0.011, +0.046)	1.36
Pasaman, West Sumatra (Indonesia)	0.85	LightGBM	0.884	+0.090 (+0.058, +0.124)	+0.005 (-0.005, +0.016)	+0.076 (+0.046, +0.105)	1.18
	0.85	CNN2D	0.907	+0.054 (+0.030, +0.082)	-0.006 (-0.018, +0.004)	+0.037 (+0.019, +0.057)	1.45
São Paulo coast (Brazil)	0.86	LightGBM	0.791	+0.166 (+0.113, +0.228)	-0.022 (-0.043, -0.001)	+0.154 (+0.100, +0.220)	1.08
	0.86	CNN2D	0.798	+0.088 (+0.045, +0.141)	-0.004 (-0.023, +0.018)	+0.065 (+0.036, +0.092)	1.37

Table S3

AEF event-level heterogeneity (between-event standard deviation tau) and prediction intervals. Detailed omission estimates are supplied in the companion CSV.

model	est	lo_hk	hi_hk	tau	pred_lo	pred_hi
LightGBM	0.088	0.062	0.114	0.050	-0.022	0.197
CNN2D	0.071	0.043	0.098	0.053	-0.044	0.186

Current embedding-only pooled contrasts. These analyses are unchanged by the optical scaling correction. Per-event inputs are bootstrap means. TOST evaluates equivalence within $\pm$0.01 AUC; a displayed 0.000 denotes p<0.001; n.a.: equivalence is tested for placebo contrasts only.

Point set	Representation / model	Contrast	k	DerSimonian–Laird (95% CI)	REML with HKSJ interval	Positive events	TOST p (DL / HKSJ)
AlphaEarth, audit points	LightGBM	event year d_0	18	+0.087 (+0.065, +0.110)	+0.088 (+0.062, +0.114)	18/18	n.a.
AlphaEarth, audit points	LightGBM	placebo	15	+0.002 (-0.003, +0.007)	+0.002 (-0.005, +0.009)	9/15	0.001 / 0.011
AlphaEarth, audit points	LightGBM	year after d_1	18	+0.104 (+0.076, +0.133)	+0.105 (+0.072, +0.137)	18/18	n.a.
AlphaEarth, audit points	LightGBM	d_0 - placebo	15	+0.085 (+0.057, +0.113)	+0.085 (+0.051, +0.120)	14/15	n.a.
AlphaEarth, audit points	CNN2D	event year d_0	18	+0.070 (+0.048, +0.093)	+0.071 (+0.043, +0.098)	16/18	n.a.
AlphaEarth, audit points	CNN2D	placebo	15	-0.002 (-0.006, +0.003)	-0.002 (-0.007, +0.003)	6/15	0.000 / 0.002
AlphaEarth, audit points	CNN2D	year after d_1	18	+0.078 (+0.052, +0.104)	+0.078 (+0.047, +0.110)	17/18	n.a.
AlphaEarth, audit points	CNN2D	d_0 - placebo	15	+0.064 (+0.035, +0.093)	+0.064 (+0.031, +0.096)	14/15	n.a.
TESSERA points	TESSERA	event year d_0	10	+0.104 (+0.073, +0.135)	+0.105 (+0.061, +0.149)	10/10	n.a.
TESSERA points	TESSERA	placebo	10	+0.003 (-0.010, +0.016)	+0.003 (-0.015, +0.020)	5/10	0.148 / 0.184
TESSERA points	TESSERA	year after d_1	10	+0.121 (+0.089, +0.154)	+0.121 (+0.091, +0.151)	10/10	n.a.
TESSERA points	TESSERA	d_0 - placebo	10	+0.103 (+0.058, +0.147)	+0.104 (+0.044, +0.163)	9/10	n.a.
TESSERA points	AlphaEarth	event year d_0	10	+0.071 (+0.047, +0.094)	+0.073 (+0.036, +0.109)	10/10	n.a.
TESSERA points	AlphaEarth	placebo	10	-0.002 (-0.010, +0.006)	-0.003 (-0.014, +0.009)	4/10	0.030 / 0.089
TESSERA points	AlphaEarth	year after d_1	10	+0.088 (+0.055, +0.121)	+0.088 (+0.052, +0.123)	10/10	n.a.
TESSERA points	AlphaEarth	d_0 - placebo	10	+0.072 (+0.044, +0.101)	+0.075 (+0.028, +0.122)	9/10	n.a.

Table S4

TESSERA audit (10 events) with AlphaEarth recomputed on the same points, folds and bootstrap resamples.

Event	f	TESSERA version	Points (ls / all)	Pre-event AUC TESSERA / AE	TESSERA event year	TESSERA placebo	TESSERA year after	AlphaEarth event year	AE - TESSERA (event year)
Mesetas (Colombia)	0.02	v1	1,990 / 5,970	0.754 / 0.855	+0.020 (-0.002, +0.044)	+0.041 (+0.023, +0.062)	+0.127 (+0.095, +0.158)	+0.006 (-0.006, +0.019)	-0.014 (-0.035, +0.008)
Jishishan (China)	0.04	v1	2,984 / 8,660	0.537 / 0.541	+0.048 (+0.010, +0.080)	+0.016 (-0.001, +0.030)	+0.082 (+0.017, +0.148)	+0.020 (+0.000, +0.041)	-0.028 (-0.050, -0.002)
Helene, southern Appalachians (USA)	0.26	v1	2,213 / 6,639	0.706 / 0.815	+0.114 (+0.087, +0.154)	-0.007 (-0.022, +0.009)	+0.175 (+0.144, +0.214)	+0.073 (+0.064, +0.084)	-0.041 (-0.078, -0.013)
Luding (China)	0.32	v1	2,675 / 7,859	0.630 / 0.705	+0.066 (+0.047, +0.086)	+0.030 (+0.004, +0.050)	+0.144 (+0.102, +0.182)	+0.086 (+0.066, +0.102)	+0.019 (-0.000, +0.037)
Fujian (China)	0.43	v1	345 / 1,036	0.748 / 0.822	+0.125 (+0.087, +0.168)	-0.029 (-0.067, +0.006)	+0.107 (+0.074, +0.145)	+0.069 (+0.050, +0.094)	-0.056 (-0.100, -0.015)
Lushan (China)	0.58	v1	1,286 / 3,858	0.763 / 0.833	+0.113 (+0.092, +0.138)	-0.023 (-0.042, -0.004)	+0.103 (+0.081, +0.130)	+0.091 (+0.071, +0.115)	-0.022 (-0.042, -0.001)
Agatha (Mexico)	0.59	v1.1-cam	2,949 / 5,213	0.685 / 0.749	+0.182 (+0.148, +0.218)	-0.006 (-0.020, +0.008)	+0.165 (+0.137, +0.197)	+0.159 (+0.126, +0.197)	-0.023 (-0.053, +0.007)
Emilia-Romagna (Italy)	0.63	v1	3,000 / 9,000	0.814 / 0.897	+0.062 (+0.050, +0.075)	+0.011 (-0.004, +0.023)	+0.049 (+0.037, +0.063)	+0.031 (+0.023, +0.039)	-0.031 (-0.045, -0.020)
Freddy (Malawi)	0.81	v1.1-cam	1,634 / 4,582	0.735 / 0.853	+0.118 (+0.088, +0.143)	+0.011 (-0.010, +0.029)	+0.097 (+0.068, +0.122)	+0.058 (+0.038, +0.079)	-0.060 (-0.082, -0.035)
São Paulo coast (Brazil)	0.86	v1.1-cam	326 / 717	0.712 / 0.791	+0.227 (+0.171, +0.284)	-0.037 (-0.068, -0.000)	+0.173 (+0.118, +0.229)	+0.167 (+0.113, +0.228)	-0.060 (-0.108, -0.017)

Table S5

Annual Sentinel-2 point composites under the two asset-scaling rules. Original 15-event samples, folds and learner settings are fixed. The primary rule applies the declared offset only where harmonization is unresolved; the alternative treats those unresolved offsets as already applied. Other assets are identical. Changes are event-year minus prior-year AUC; intervals use the same 1,000 spatial-cluster resamples. The last contrast subtracts the primary increment from the alternative increment. Negative effects remain in pooling. Scene-point fractions describe optical sampling, not foundation-model information weights.

Event	Primary AUC prior / event	Primary change (95% CI)	Alternative change (95% CI)	Alternative - primary (95% CI)	Positive / control
Chittagong	0.559 / 0.862	+0.304 (+0.269, +0.342)	+0.332 (+0.301, +0.362)	+0.028 (+0.008, +0.047)	448 / 896
São Paulo	0.285 / 0.784	+0.499 (+0.326, +0.667)	+0.494 (+0.321, +0.664)	-0.005 (-0.040, +0.031)	82 / 89
Fujian	0.602 / 0.749	+0.147 (+0.037, +0.259)	+0.149 (+0.063, +0.247)	+0.002 (-0.043, +0.046)	91 / 182
Agatha	0.543 / 0.625	+0.081 (+0.022, +0.140)	+0.068 (+0.005, +0.128)	-0.014 (-0.055, +0.023)	964 / 733
Freddy	0.554 / 0.693	+0.139 (+0.063, +0.203)	+0.139 (+0.063, +0.203)	+0.000 (+0.000, +0.000)	523 / 862
Nalgae (Mindanao)	0.522 / 0.461	-0.061 (-0.165, +0.065)	+0.004 (-0.116, +0.175)	+0.065 (-0.058, +0.203)	56 / 112
Luzon	0.547 / 0.757	+0.209 (+0.184, +0.237)	+0.202 (+0.179, +0.225)	-0.008 (-0.027, +0.013)	806 / 1613
Northern Vietnam	0.540 / 0.714	+0.173 (+0.127, +0.214)	+0.177 (+0.130, +0.220)	+0.004 (-0.019, +0.027)	562 / 1055
Lushan	0.628 / 0.779	+0.151 (+0.095, +0.208)	+0.155 (+0.098, +0.212)	+0.004 (-0.018, +0.029)	437 / 517
Mesetas	0.565 / 0.478	-0.088 (-0.160, -0.001)	-0.088 (-0.160, -0.001)	+0.000 (+0.000, +0.000)	472 / 620
Palu	0.442 / 0.607	+0.165 (+0.089, +0.238)	+0.165 (+0.089, +0.238)	+0.000 (+0.000, +0.000)	332 / 677
Pasaman	0.509 / 0.732	+0.223 (+0.113, +0.317)	+0.225 (+0.113, +0.323)	+0.001 (-0.019, +0.023)	100 / 219
Eastern Iburi	0.386 / 0.433	+0.047 (+0.015, +0.080)	+0.047 (+0.015, +0.080)	+0.000 (+0.000, +0.000)	2008 / 3501
Luding	0.551 / 0.519	-0.032 (-0.072, +0.003)	-0.027 (-0.069, +0.010)	+0.005 (-0.005, +0.017)	2098 / 3834
Emilia-Romagna	0.710 / 0.646	-0.064 (-0.100, -0.027)	-0.042 (-0.076, -0.009)	+0.022 (+0.010, +0.033)	3000 / 5997

Nalgae's point estimate crosses zero, but its paired difference interval crosses zero too. In that event, 5/12 selected 2022 scenes are unresolved and supply 460/1,289 (35.7%) valid scene-point observations on the fixed sample support; both pre-event years and 2023 have no unresolved scenes. Across all events and years, the scene and observation denominators are in annual_s2_unresolved_exposure.csv, with scene identities and local raw-chunk hashes in annual_s2_observation_sources.csv.

Table S6

Optical common-support counts. Each event starts with 1,100 positive objects and 2,200 controls. The companion flow table records every sequential exclusion and the set-intersection table verifies which populations overlap; ratios between different support sets are not reported as retention rates.

event	subset	n_pos	n_neg	status
IBU2018	curve	474	1008	estimated
IBU2018	curve_all	474	1008	estimated
IBU2018	season	281	972	estimated
IBU2018	allten	0	0	ineligible: class below 100
IBU2018	gate	489	1291	estimated
MKH2018	curve	1080	2089	estimated
MKH2018	curve_all	1080	2089	estimated
MKH2018	season	315	442	estimated
MKH2018	allten	225	326	estimated
MKH2018	gate	1079	2101	estimated

Table S7

Absolute AUC for all four seasonal endpoints. Main AUC averages independently evaluated three-date draws; its 95% interval uses joint spatial and draw resampling. Seed 0 is the single fixed-three-date-set sensitivity. Fold-level scores and AUCs, including values below 0.5, are archived without score reversal. Other optical tables use IBU 2018 for Eastern Iburi and MKH 2018 for Mangkhut.

Event	Year / cutoff	Mean AUC	CI lower	CI upper	Seed-0 AUC	Landslides	Controls
Eastern Iburi	2017 / -1 d	0.429	0.381	0.485	0.394	281	972
Eastern Iburi	2017 / 60 d	0.397	0.355	0.450	0.401	281	972
Eastern Iburi	2018 / -1 d	0.420	0.373	0.480	0.460	281	972
Eastern Iburi	2018 / 60 d	0.811	0.762	0.847	0.819	281	972
Mangkhut	2017 / -1 d	0.516	0.469	0.554	0.509	315	442
Mangkhut	2017 / 60 d	0.596	0.549	0.635	0.586	315	442
Mangkhut	2018 / -1 d	0.475	0.437	0.515	0.459	315	442
Mangkhut	2018 / 60 d	0.786	0.755	0.814	0.767	315	442

Table S8

Optical paired contrasts. The scene-gate difference is computed on the same eligible points and compares the gated with the pixel-only cutoff increment. The allten rows, where eligible, use their own support.

event	subset	contrast	effect_95CI	seed0
IBU2018	curve	y2018_d-30-y2018_d-1	+0.002 (-0.036 to +0.043)	0.000
IBU2018	curve	y2018_d7-y2018_d-1	+0.000 (+0.000 to +0.000)	0.000
IBU2018	curve	y2018_d30-y2018_d-1	+0.019 (-0.006 to +0.043)	-0.017
IBU2018	curve	y2018_d60-y2018_d-1	+0.337 (+0.289 to +0.380)	0.329
IBU2018	curve_all	y2018_d-30-y2018_d-1	+0.020 (-0.036 to +0.072)	0.020
IBU2018	curve_all	y2018_d7-y2018_d-1	+0.000 (+0.000 to +0.000)	0.000
IBU2018	curve_all	y2018_d30-y2018_d-1	+0.038 (+0.007 to +0.065)	0.038
IBU2018	curve_all	y2018_d60-y2018_d-1	+0.391 (+0.325 to +0.450)	0.391
IBU2018	season	y2017_d60-y2017_d-1	-0.032 (-0.075 to +0.012)	0.007
IBU2018	season	y2018_d60-y2018_d-1	+0.390 (+0.324 to +0.434)	0.359
IBU2018	season	DID_d60	+0.423 (+0.353 to +0.479)	0.352
IBU2018	gate	y2018_d60-y2018_d-1	+0.338 (+0.281 to +0.384)	0.318
IBU2018	gate	y2018_d60_gate-y2018_d-1_gate	+0.339 (+0.283 to +0.388)	0.342
IBU2018	gate	gate_change_in_event_increment	+0.001 (-0.017 to +0.019)	0.023
MKH2018	curve	y2018_d-30-y2018_d-1	+0.006 (-0.015 to +0.027)	0.035
MKH2018	curve	y2018_d7-y2018_d-1	+0.002 (-0.011 to +0.016)	0.023
MKH2018	curve	y2018_d30-y2018_d-1	+0.178 (+0.150 to +0.207)	0.210
MKH2018	curve	y2018_d60-y2018_d-1	+0.293 (+0.258 to +0.329)	0.315
MKH2018	curve_all	y2018_d-30-y2018_d-1	+0.027 (+0.001 to +0.053)	0.027
MKH2018	curve_all	y2018_d7-y2018_d-1	+0.012 (-0.011 to +0.035)	0.012
MKH2018	curve_all	y2018_d30-y2018_d-1	+0.284 (+0.230 to +0.333)	0.284
MKH2018	curve_all	y2018_d60-y2018_d-1	+0.345 (+0.305 to +0.390)	0.345
MKH2018	season	y2017_d60-y2017_d-1	+0.080 (+0.031 to +0.136)	0.077
MKH2018	season	y2018_d60-y2018_d-1	+0.311 (+0.267 to +0.357)	0.308
MKH2018	season	DID_d60	+0.231 (+0.164 to +0.293)	0.231
MKH2018	allten	y2017_d-30-y2017_d-1	+0.012 (-0.027 to +0.048)	-0.014
MKH2018	allten	y2017_d7-y2017_d-1	-0.016 (-0.047 to +0.017)	-0.039
MKH2018	allten	y2017_d30-y2017_d-1	-0.041 (-0.086 to +0.006)	-0.120
MKH2018	allten	y2017_d60-y2017_d-1	+0.085 (+0.030 to +0.138)	0.046
MKH2018	allten	y2018_d-30-y2018_d-1	+0.031 (-0.008 to +0.071)	0.051
MKH2018	allten	y2018_d7-y2018_d-1	+0.017 (-0.021 to +0.062)	0.021
MKH2018	allten	y2018_d30-y2018_d-1	+0.193 (+0.146 to +0.242)	0.149
MKH2018	allten	y2018_d60-y2018_d-1	+0.321 (+0.271 to +0.370)	0.277
MKH2018	allten	DID_d-30	+0.020 (-0.043 to +0.087)	0.065
MKH2018	allten	DID_d7	+0.033 (-0.019 to +0.091)	0.060
MKH2018	allten	DID_d30	+0.234 (+0.170 to +0.294)	0.269
MKH2018	allten	DID_d60	+0.236 (+0.170 to +0.308)	0.231
MKH2018	gate	y2018_d60-y2018_d-1	+0.295 (+0.265 to +0.327)	0.320
MKH2018	gate	y2018_d60_gate-y2018_d-1_gate	+0.297 (+0.266 to +0.333)	0.308
MKH2018	gate	gate_change_in_event_increment	+0.002 (-0.013 to +0.016)	-0.011

Table S9

Distinct dates in the union of ten current draws, among all points individually eligible in each window. Each draw uses exactly three dates and is evaluated separately. Counts describe the date pool across draws, not a single prediction's information budget. The superseded prediction-ensemble date audit is retained in the versioned data files.

Event	Window	Points	Minimum	Median	Maximum
IBU2018	y2017_d-1	2761	3	3.000	5
IBU2018	y2017_d30	465	3	3.000	4
IBU2018	y2017_d60	2140	3	3.000	6
IBU2018	y2017_d7	2761	3	3.000	5
IBU2018	y2018_d-1	1876	3	3.000	6
IBU2018	y2018_d-30	2369	3	3.000	6
IBU2018	y2018_d30	2132	3	4.000	7
IBU2018	y2018_d60	3027	3	5.000	9
IBU2018	y2018_d7	1876	3	3.000	6
MKH2018	y2017_d-1	3006	3	4.000	8
MKH2018	y2017_d-30	3158	3	5.000	10
MKH2018	y2017_d30	1293	3	3.000	6
MKH2018	y2017_d60	812	3	3.000	5
MKH2018	y2017_d7	2405	3	4.000	7
MKH2018	y2018_d-1	3181	3	6.000	14
MKH2018	y2018_d-30	3249	3	7.000	16
MKH2018	y2018_d30	3279	3	8.000	17
MKH2018	y2018_d60	3300	3	10.000	21
MKH2018	y2018_d7	3223	3	6.000	14

Table S10

Current retrospective scheme levels and their paired contrasts. Intervals condition on trained models.

region	scheme	AUC_95CI	n_pos	n_neg
NC	B0	0.726 (0.706–0.745)	2025	3685
NC	H	0.585 (0.538–0.624)	2025	3685
NC	B1	0.697 (0.661–0.729)	2025	3685
NC	B2	0.774 (0.754–0.795)	2025	3685
NC	B3	0.756 (0.725–0.784)	2025	3685
NC	B0_AEF	0.777 (0.756–0.798)	2025	3685
NC	diagnostic_post	0.830 (0.812–0.848)	2025	3685
Lushan	B0	0.568 (0.514–0.630)	1286	2572
Lushan	H	0.724 (0.666–0.771)	1286	2572
Lushan	B1	0.728 (0.667–0.775)	1286	2572
Lushan	B2	0.594 (0.535–0.654)	1286	2572
Lushan	B3	0.736 (0.675–0.780)	1286	2572
Lushan	B0_AEF	0.600 (0.542–0.659)	1286	2572
Lushan	diagnostic_post	0.713 (0.660–0.764)	1286	2572

region	contrast	effect_95CI
NC	B3-B1	+0.059 (+0.044 to +0.077)
NC	B1-B0	-0.030 (-0.065 to +0.001)
NC	B2-B0	+0.048 (+0.029 to +0.068)
NC	B0_AEF-B0	+0.051 (+0.033 to +0.067)
NC	diagnostic_post-B2	+0.056 (+0.042 to +0.069)
Lushan	B3-B1	+0.008 (-0.007 to +0.022)
Lushan	B1-B0	+0.160 (+0.070 to +0.238)
Lushan	B2-B0	+0.026 (-0.030 to +0.073)
Lushan	B0_AEF-B0	+0.032 (-0.026 to +0.081)
Lushan	diagnostic_post-B2	+0.119 (+0.097 to +0.142)

Table S11

History-operator and training-control sensitivities, followed by near/far support counts for the main designs. Uniform 30 m is the previous operator. The identity operator removes only a training positive's own source, keeping all legitimate historical neighbours at test time. A date-qualified training set does not establish that the inventory version was publicly available in the target year.

design	B0	H	B1	B2	B3	B0_AEF
NC_strict_identity	0.726	0.585	0.697	0.774	0.756	0.777
NC_legacy_identity	0.731	0.597	0.699	0.778	0.751	0.782
NC_legacy_radius30	0.731	0.597	0.699	0.778	0.749	0.782
Lushan_legacy_identity	0.568	0.724	0.728	0.594	0.736	0.600
Lushan_legacy_radius30	0.568	0.714	0.725	0.594	0.733	0.600

design	subset	n_pos	n_neg	estimated
NC_strict_identity	all	2025	3685	True
NC_strict_identity	near_le100m	70	25	False
NC_strict_identity	far_gt100m	1955	3660	True
NC_strict_identity	post_diagnostic_common	2025	3685	True
Lushan_legacy_identity	all	1286	2572	True
Lushan_legacy_identity	near_le100m	608	319	True
Lushan_legacy_identity	far_gt100m	678	2253	True
Lushan_legacy_identity	post_diagnostic_common	1286	2572	True

region	subset	contrast	effect_95CI	n_pos	n_neg
NC	far_gt100m	B3-B1	+0.061 (+0.046 to +0.079)	1955	3660
NC	far_gt100m	B1-B0	-0.032 (-0.067 to +0.000)	1955	3660
NC	far_gt100m	B2-B0	+0.048 (+0.028 to +0.069)	1955	3660
NC	far_gt100m	B0_AEF-B0	+0.051 (+0.033 to +0.069)	1955	3660
Lushan	near_le100m	B3-B1	+0.013 (-0.036 to +0.056)	608	319
Lushan	near_le100m	B1-B0	+0.124 (+0.064 to +0.180)	608	319
Lushan	near_le100m	B2-B0	+0.025 (-0.045 to +0.075)	608	319
Lushan	near_le100m	B0_AEF-B0	+0.037 (-0.034 to +0.090)	608	319
Lushan	far_gt100m	B3-B1	+0.015 (-0.015 to +0.042)	678	2253
Lushan	far_gt100m	B1-B0	+0.033 (-0.046 to +0.118)	678	2253
Lushan	far_gt100m	B2-B0	-0.005 (-0.066 to +0.055)	678	2253
Lushan	far_gt100m	B0_AEF-B0	-0.006 (-0.066 to +0.058)	678	2253

Table S12

Map event-year differences with current binary ROC-AUC and area-capture definitions. Capture changes are fractions (multiply by 100 for percentage points); denominators are the specified evaluated domains.

event	domain	model	cap10	cap10_lo	cap10_hi	auc	auc_lo	auc_hi
RER2023	legacy_target_conditioned	LightGBM	0.158	0.137	0.180	0.050	0.043	0.060
RER2023	legacy_target_conditioned	CNN2D	0.104	0.080	0.127	0.029	0.022	0.036
GDCLD_LUS2022	legacy_target_conditioned	LightGBM	0.257	0.212	0.295	0.103	0.082	0.127
GDCLD_LUS2022	legacy_target_conditioned	CNN2D	0.248	0.191	0.306	0.094	0.073	0.122
GDCLD_MES2019	legacy_target_conditioned	LightGBM	0.033	0.002	0.057	0.005	-0.004	0.014
GDCLD_MES2019	legacy_target_conditioned	CNN2D	0.045	0.014	0.073	0.012	0.002	0.021
GDCLD_PAL2018	legacy_target_conditioned	LightGBM	0.248	0.177	0.311	0.136	0.093	0.176
GDCLD_PAL2018	legacy_target_conditioned	CNN2D	0.295	0.190	0.371	0.142	0.086	0.191
GDCLD_SUM2022	legacy_target_conditioned	LightGBM	0.281	0.196	0.350	0.147	0.104	0.200
GDCLD_SUM2022	legacy_target_conditioned	CNN2D	0.161	0.089	0.233	0.089	0.050	0.127
IBU2018	legacy_target_conditioned	LightGBM	0.387	0.331	0.447	0.299	0.266	0.332
IBU2018	legacy_target_conditioned	CNN2D	0.458	0.341	0.581	0.277	0.230	0.329
JIS2023	legacy_target_conditioned	LightGBM	0.074	0.046	0.102	0.037	0.021	0.053
JIS2023	legacy_target_conditioned	CNN2D	0.052	0.018	0.080	0.013	-0.007	0.033
LUD2022	legacy_target_conditioned	LightGBM	0.315	0.262	0.348	0.131	0.106	0.154
LUD2022	legacy_target_conditioned	CNN2D	0.336	0.274	0.382	0.132	0.112	0.155
MKH2018	legacy_target_conditioned	LightGBM	0.254	0.218	0.286	0.101	0.078	0.122
MKH2018	legacy_target_conditioned	CNN2D	0.247	0.178	0.300	0.105	0.060	0.142
FL2023	administrative_common_support_P2	LightGBM	0.193	0.143	0.254	0.108	0.079	0.141
FL2023	administrative_common_support_P2	CNN2D	0.103	0.051	0.154	0.088	0.059	0.117

Additional sensitivity and representation evidence

Table S13

Training-year × prediction-year decomposition per event (AlphaEarth). AUC $a \rightarrow b$ is the out-of-fold AUC of models trained with year a inputs and applied with year b inputs. Components are relative to the prior-year model (Y-1→Y-1), with 95% cluster-bootstrap CIs.

Event	f	Model	AUC Y-1→Y-1	AUC Y-1→Y	AUC Y→Y-1	AUC Y→Y	Prediction-time component	Training component	Event-year increment
Mesetas (Colombia)	0.02	LightGBM	0.855	0.848	0.834	0.861	-0.007 (-0.017, +0.002)	-0.021 (-0.037, -0.003)	+0.006 (-0.006, +0.019)
	0.02	CNN2D	0.878	0.870	0.865	0.897	-0.007 (-0.022, +0.010)	-0.013 (-0.025, +0.000)	+0.019 (+0.007, +0.032)
Jishishan (China)	0.04	LightGBM	0.591	0.568	0.542	0.617	-0.023 (-0.048, +0.010)	-0.048 (-0.062, -0.034)	+0.026 (+0.004, +0.048)
	0.04	CNN2D	0.734	0.656	0.671	0.717	-0.078 (-0.131, -0.014)	-0.063 (-0.130, -0.008)	-0.017 (-0.056, +0.016)
Nalgae, Mindanao (Philippines)	0.18	LightGBM	0.804	0.801	0.770	0.839	-0.003 (-0.027, +0.018)	-0.034 (-0.061, -0.003)	+0.036 (+0.016, +0.064)
	0.18	CNN2D	0.768	0.754	0.761	0.753	-0.013 (-0.034, +0.007)	-0.006 (-0.029, +0.018)	-0.015 (-0.044, +0.015)
Helene, southern Appalachians (USA)	0.26	LightGBM	0.815	0.849	0.795	0.888	+0.034 (+0.026, +0.043)	-0.020 (-0.031, -0.010)	+0.073 (+0.064, +0.084)
	0.26	CNN2D	0.801	0.799	0.760	0.866	-0.002 (-0.017, +0.010)	-0.041 (-0.064, -0.011)	+0.065 (+0.055, +0.078)
Palu (Indonesia)	0.26	LightGBM	0.720	0.705	0.695	0.835	-0.015 (-0.050, +0.018)	-0.025 (-0.054, +0.007)	+0.115 (+0.081, +0.154)
	0.26	CNN2D	0.737	0.768	0.745	0.867	+0.031 (-0.004, +0.078)	+0.009 (-0.028, +0.046)	+0.131 (+0.085, +0.177)
Mangkhut, Itogon (Philippines)	0.29	LightGBM	0.818	0.832	0.745	0.873	+0.014 (+0.002, +0.026)	-0.073 (-0.103, -0.045)	+0.055 (+0.039, +0.069)
	0.29	CNN2D	0.763	0.835	0.728	0.870	+0.072 (+0.024, +0.119)	-0.035 (-0.089, +0.017)	+0.107 (+0.057, +0.159)
Eastern Iburi (Japan)	0.32	LightGBM	0.829	0.761	0.702	0.926	-0.068 (-0.110, -0.030)	-0.127 (-0.176, -0.076)	+0.098 (+0.075, +0.122)
	0.32	CNN2D	0.830	0.726	0.587	0.948	-0.104 (-0.159, -0.054)	-0.243 (-0.304, -0.175)	+0.118 (+0.078, +0.156)
Luding (China)	0.32	LightGBM	0.757	0.760	0.720	0.842	+0.003 (-0.010, +0.017)	-0.037 (-0.062, -0.008)	+0.085 (+0.066, +0.100)
	0.32	CNN2D	0.796	0.798	0.656	0.903	+0.001 (-0.048, +0.033)	-0.140 (-0.194, -0.067)	+0.107 (+0.085, +0.128)
Chittagong (Bangladesh)	0.38	LightGBM	0.808	0.831	0.768	0.936	+0.023 (+0.015, +0.031)	-0.040 (-0.067, -0.013)	+0.128 (+0.106, +0.148)
	0.38	CNN2D	0.804	0.832	0.737	0.894	+0.028 (+0.015, +0.037)	-0.067 (-0.092, -0.040)	+0.090 (+0.070, +0.110)
Northern Vietnam	0.41	LightGBM	0.678	0.702	0.612	0.820	+0.023 (-0.001, +0.051)	-0.067 (-0.098, -0.032)	+0.141 (+0.108, +0.173)
	0.41	CNN2D	0.721	0.727	0.662	0.807	+0.007 (-0.019, +0.028)	-0.059 (-0.095, -0.027)	+0.086 (+0.045, +0.120)
Fujian (China)	0.43	LightGBM	0.822	0.801	0.789	0.890	-0.020 (-0.040, +0.001)	-0.032 (-0.061, +0.002)	+0.069 (+0.050, +0.094)
	0.43	CNN2D	0.800	0.794	0.761	0.825	-0.006 (-0.030, +0.020)	-0.039 (-0.062, -0.006)	+0.025 (-0.005, +0.053)
Luzon (Philippines)	0.43	LightGBM	0.727	0.750	0.687	0.927	+0.023 (+0.004, +0.041)	-0.040 (-0.056, -0.019)	+0.200 (+0.178, +0.224)
	0.43	CNN2D	0.729	0.740	0.656	0.931	+0.011 (-0.009, +0.031)	-0.073 (-0.100, -0.045)	+0.202 (+0.179, +0.230)
Lushan (China)	0.58	LightGBM	0.833	0.869	0.823	0.924	+0.035 (+0.016, +0.057)	-0.010 (-0.028, +0.006)	+0.091 (+0.071, +0.115)
	0.58	CNN2D	0.842	0.860	0.849	0.921	+0.018 (+0.004, +0.034)	+0.006 (-0.005, +0.017)	+0.079 (+0.056, +0.106)
Agatha (Mexico)	0.59	LightGBM	0.766	0.738	0.667	0.910	-0.028 (-0.045, -0.010)	-0.100 (-0.129, -0.072)	+0.144 (+0.116, +0.172)
	0.59	CNN2D	0.789	0.721	0.676	0.882	-0.068 (-0.104, -0.027)	-0.113 (-0.161, -0.068)	+0.093 (+0.066, +0.119)
Emilia-Romagna (Italy)	0.63	LightGBM	0.908	0.888	0.844	0.933	-0.020 (-0.026, -0.014)	-0.064 (-0.078, -0.053)	+0.025 (+0.019, +0.031)
	0.63	CNN2D	0.935	0.837	0.870	0.951	-0.098 (-0.118, -0.078)	-0.065 (-0.081, -0.052)	+0.015 (+0.011, +0.021)
Freddy (Malawi)	0.81	LightGBM	0.853	0.846	0.838	0.912	-0.007 (-0.018, +0.005)	-0.016 (-0.030, -0.002)	+0.058 (+0.038, +0.079)
	0.81	CNN2D	0.833	0.826	0.810	0.871	-0.008 (-0.020, +0.008)	-0.023 (-0.044, -0.004)	+0.038 (+0.015, +0.064)
Pasaman, West Sumatra (Indonesia)	0.85	LightGBM	0.884	0.936	0.863	0.974	+0.052 (+0.033, +0.072)	-0.021 (-0.043, -0.001)	+0.090 (+0.058, +0.124)
	0.85	CNN2D	0.907	0.932	0.839	0.960	+0.025 (+0.011, +0.043)	-0.068 (-0.123, -0.013)	+0.053 (+0.030, +0.082)
São Paulo coast (Brazil)	0.86	LightGBM	0.791	0.748	0.724	0.957	-0.042 (-0.069, -0.011)	-0.066 (-0.118, -0.005)	+0.167 (+0.113, +0.228)
	0.86	CNN2D	0.798	0.761	0.760	0.885	-0.037 (-0.060, -0.013)	-0.038 (-0.085, +0.020)	+0.088 (+0.045, +0.141)

Table S14

Increments for the year after next (Y+2; 17 events; Helene has no 2026 product). The decay ratio d_2/d_1 is per event; the pooled decay uses events with a visible year-after signal (Text S5).

Event	f	Model	Event year d0	Year after d1	Year after next d2	d2/d1	Year-after signal visible
Mesetas (Colombia)	0.02	CNN2D	+0.020	+0.081	+0.053	0.65	yes
Mesetas (Colombia)	0.02	LightGBM	+0.006	+0.090	+0.062	0.69	yes
Jishishan (China)	0.04	CNN2D	-0.017	+0.040	+0.073	1.84	yes
Jishishan (China)	0.04	LightGBM	+0.026	+0.026	+0.021	0.80	yes
Nalgae, Mindanao (Philippines)	0.18	CNN2D	-0.015	-0.024	-0.007	0.29	no
Nalgae, Mindanao (Philippines)	0.18	LightGBM	+0.036	+0.017	+0.042	2.53	no
Palu (Indonesia)	0.26	CNN2D	+0.131	+0.209	+0.205	0.98	yes
Palu (Indonesia)	0.26	LightGBM	+0.115	+0.256	+0.242	0.95	yes
Mangkhut, Itogon (Philippines)	0.29	CNN2D	+0.107	+0.071	+0.013	0.19	yes
Mangkhut, Itogon (Philippines)	0.29	LightGBM	+0.055	+0.057	+0.001	0.02	yes
Eastern Iburi (Japan)	0.32	CNN2D	+0.118	+0.152	+0.152	1.00	yes
Eastern Iburi (Japan)	0.32	LightGBM	+0.098	+0.152	+0.150	0.99	yes
Luding (China)	0.32	CNN2D	+0.107	+0.134	+0.118	0.88	yes
Luding (China)	0.32	LightGBM	+0.085	+0.139	+0.126	0.91	yes
Chittagong (Bangladesh)	0.38	CNN2D	+0.090	+0.061	+0.022	0.37	yes
Chittagong (Bangladesh)	0.38	LightGBM	+0.128	+0.105	+0.069	0.65	yes
Northern Vietnam	0.41	CNN2D	+0.086	+0.075	+0.021	0.27	yes
Northern Vietnam	0.41	LightGBM	+0.141	+0.145	+0.081	0.56	yes
Fujian (China)	0.43	CNN2D	+0.025	+0.016	+0.013	0.80	no
Fujian (China)	0.43	LightGBM	+0.069	+0.075	+0.046	0.61	yes
Luzon (Philippines)	0.43	CNN2D	+0.202	+0.209	+0.162	0.77	yes
Luzon (Philippines)	0.43	LightGBM	+0.200	+0.219	+0.175	0.80	yes
Lushan (China)	0.58	CNN2D	+0.079	+0.080	+0.064	0.80	yes
Lushan (China)	0.58	LightGBM	+0.091	+0.090	+0.073	0.81	yes
Agatha (Mexico)	0.59	CNN2D	+0.093	+0.054	+0.025	0.47	yes
Agatha (Mexico)	0.59	LightGBM	+0.144	+0.114	+0.070	0.61	yes
Emilia-Romagna (Italy)	0.63	CNN2D	+0.015	+0.017	+0.012	0.71	yes
Emilia-Romagna (Italy)	0.63	LightGBM	+0.025	+0.024	+0.015	0.64	yes
Freddy (Malawi)	0.81	CNN2D	+0.038	+0.028	+0.017	0.60	yes
Freddy (Malawi)	0.81	LightGBM	+0.058	+0.044	+0.024	0.55	yes
Pasaman, West Sumatra (Indonesia)	0.85	CNN2D	+0.053	+0.037	+0.018	0.49	yes
Pasaman, West Sumatra (Indonesia)	0.85	LightGBM	+0.090	+0.076	+0.064	0.84	yes
São Paulo coast (Brazil)	0.86	CNN2D	+0.088	+0.064	+0.045	0.70	yes
São Paulo coast (Brazil)	0.86	LightGBM	+0.167	+0.155	+0.140	0.91	yes

Recovery adjustment of the AEF exposure model. The year-after product covers lags f to $f + 1$ years. With exponential recovery at rate λ, its signal is proportional to $\exp(-\lambda f)$, so the ratio d_0/d_1 contains a factor $\exp(\lambda f)$. We estimated λ from the products of the year after next (Y+2, 17 events) as $\lambda = -\ln q$, with $q = \Sigma d_2/\Sigma d_1$ over events whose year-after increment is distinguishable from zero. The interval for q comes from an event bootstrap with 2,000 resamples. We then refitted the joint model with d_1 multiplied by $\exp(\lambda f)$, its variance by $\exp(2\lambda f)$ and the covariance by $\exp(\lambda f)$.

Quantity	Point LightGBM	Patch CNN2D
Decay ratio q (event bootstrap 95% CI)	0.770 (0.661–0.854)	0.762 (0.592–0.898)
λ (per year)	0.26	0.27
Unadjusted: slope p; A; f_{50}	0.0005; 1.16; 0.24	0.0003; 1.14; 0.26
Adjusted: slope p; A; f_{50}	0.004; 0.96; 0.23	0.002; 0.99; 0.26
Adjusted with λ at the CI ends: slope p; A	0.002–0.013; 0.87–1.03	0.001–0.011; 0.87–1.08

Table S15

Controlled re-analysis of the setting of Cheng et al. [3]. n.a.: not computed for the reconstructed protocol. **P1:** random 70:30 split; five seeds; t-based CIs. **P2:** spatial 5-fold cross-validation with a 500 m buffer; 30-cluster bootstrap. **P1 paper:** a reconstructed protocol with the documented factor differences. **LCF:** our six terrain factors; the original study used 14.

Protocol	Sample	Model	AUC LCF	AUC AE2022 (pre-event)	AUC AE2023 (event year)	Event year (AE2023 - AE2022)	Placebo (AE2022 - AE2021)	Pre-event vs LCF (AE2022 - LCF)
P1	2,614 + 2,614	CNN1D	0.864	0.918	0.953	+0.034 (+0.027, +0.041)	+0.000 (-0.008, +0.008)	+0.055 (+0.043, +0.067)
P1	2,614 + 2,614	CNN2D	0.895	0.944	0.961	+0.017 (+0.012, +0.022)	-0.001 (-0.009, +0.008)	+0.048 (+0.038, +0.059)
P1	2,614 + 2,614	ViT	0.904	0.947	0.967	+0.020 (+0.012, +0.028)	-0.002 (-0.011, +0.007)	+0.043 (+0.033, +0.053)
P1	2,614 + 2,614	LightGBM	0.860	0.924	0.956	+0.032 (+0.025, +0.038)	+0.000 (-0.003, +0.004)	+0.065 (+0.055, +0.075)
P1	10,365 + 10,365	CNN1D	0.881	0.943	0.970	+0.027 (+0.024, +0.031)	+0.000 (-0.002, +0.002)	+0.061 (+0.056, +0.066)
P1	10,365 + 10,365	CNN2D	0.916	0.969	0.980	+0.011 (+0.008, +0.013)	+0.001 (-0.004, +0.006)	+0.053 (+0.049, +0.057)
P1	10,365 + 10,365	ViT	0.948	0.973	0.986	+0.013 (+0.009, +0.016)	-0.002 (-0.004, +0.001)	+0.025 (+0.021, +0.030)
P1	10,365 + 10,365	LightGBM	0.884	0.942	0.969	+0.027 (+0.024, +0.030)	-0.002 (-0.003, -0.001)	+0.058 (+0.055, +0.061)
P2	2,614 + 2,614	CNN1D	0.792	0.838	0.915	+0.076 (+0.039, +0.117)	-0.006 (-0.018, +0.006)	+0.048 (+0.028, +0.074)
P2	2,614 + 2,614	CNN2D	0.818	0.858	0.902	+0.042 (+0.009, +0.077)	+0.002 (-0.017, +0.021)	+0.040 (+0.015, +0.070)
P2	2,614 + 2,614	ViT	0.809	0.834	0.897	+0.064 (+0.029, +0.107)	-0.010 (-0.028, +0.007)	+0.037 (+0.005, +0.077)
P2	2,614 + 2,614	LightGBM	0.783	0.829	0.913	+0.084 (+0.044, +0.129)	-0.003 (-0.015, +0.009)	+0.046 (+0.015, +0.078)
P2	10,365 + 10,365	CNN1D	0.800	0.857	0.929	+0.069 (+0.035, +0.108)	-0.012 (-0.030, +0.001)	+0.060 (+0.036, +0.089)
P2	10,365 + 10,365	CNN2D	0.830	0.861	0.920	+0.057 (+0.029, +0.089)	+0.003 (-0.010, +0.017)	+0.038 (+0.009, +0.072)
P2	10,365 + 10,365	ViT	0.812	0.851	0.936	+0.086 (+0.046, +0.132)	-0.011 (-0.030, +0.004)	+0.034 (+0.007, +0.063)
P2	10,365 + 10,365	LightGBM	0.808	0.848	0.928	+0.079 (+0.041, +0.121)	-0.009 (-0.022, +0.002)	+0.041 (+0.014, +0.068)
P1paper	2,614 + 2,614	CNN1D	0.868	0.928	0.958	+0.031 (+0.023, +0.038)	n.a.	+0.059 (+0.048, +0.070)
P1paper	2,614 + 2,614	CNN2D	0.910	0.953	0.969	+0.015 (+0.012, +0.019)	n.a.	+0.044 (+0.038, +0.049)
P1paper	2,614 + 2,614	ViT	0.919	0.955	0.972	+0.016 (+0.011, +0.022)	n.a.	+0.037 (+0.031, +0.043)

P1 paper selects batch size and learning rate using the same 30% split on which its AUC is reported. It reproduces that selection procedure and is not an independent test estimate; P1 and P2 use inner validation for early stopping. The principal annual audit uses fixed settings.

Table S16

Cross-year stability of the two embedding products at control points. Stability index = (c_same - c_rand)/(1 - c_rand).

Event (control points)	Years	AlphaEarth cosine, same site	AlphaEarth cosine, random pairs	AlphaEarth stability index	TESSERA cosine, same site	TESSERA cosine, random pairs	TESSERA stability index
Helene, southern Appalachians (USA)	2022→2023	0.982	0.732	0.933	0.914	0.698	0.715
Helene, southern Appalachians (USA)	2023→2024	0.983	0.742	0.935	0.908	0.704	0.689
Emilia-Romagna (Italy)	2021→2022	0.973	0.584	0.936	0.910	0.516	0.814
Jishishan (China)	2021→2022	0.977	0.688	0.925	0.860	0.638	0.613
Lushan (China)	2020→2021	0.979	0.698	0.930	0.873	0.701	0.578
Mesetas (Colombia)	2017→2018	0.965	0.671	0.894	0.840	0.715	0.439
Luding (China)	2020→2021	0.984	0.612	0.958	0.888	0.630	0.698
Fujian (China)	2021→2022	0.950	0.746	0.801	0.851	0.711	0.484

Table S17

Typhoon Mangkhut: event-year and year-after increments after excluding points near mapped mining areas [54].

Points kept	Model	Points (landslides)	Event year d0	Year after d1	Ratio d0/d1 (95% range)
all	LightGBM	3,300 (1,100)	+0.055 (+0.039, +0.069)	+0.057 (+0.041, +0.072)	0.97 (0.82–1.12)
all	CNN2D	3,300 (1,100)	+0.107 (+0.057, +0.159)	+0.071 (+0.035, +0.103)	1.52 (1.27–1.86)
> 500 m from mapped mining areas	LightGBM	3,227 (1,058)	+0.056 (+0.036, +0.072)	+0.065 (+0.045, +0.085)	0.85 (0.70–1.00)
> 500 m from mapped mining areas	CNN2D	3,227 (1,058)	+0.092 (+0.047, +0.141)	+0.073 (+0.036, +0.110)	1.26 (1.00–1.58)
> 1000 m from mapped mining areas	LightGBM	3,071 (984)	+0.052 (+0.033, +0.070)	+0.059 (+0.038, +0.079)	0.89 (0.73–1.09)
> 1000 m from mapped mining areas	CNN2D	3,071 (984)	+0.094 (+0.053, +0.138)	+0.064 (+0.028, +0.093)	1.48 (1.20–2.09)

Table S18

Versions of the annual embedding files used. On 16 October 2026 every source file behind the data used was queried with an HTTP HEAD request; all requests returned status 200. Sizes are those of the complete source files, of which only small parts were read. The full lists, with the ETag, size and last-modified date of every file, are Supplementary Data S1 (AlphaEarth) and S2 (TESSERA).

Product	Version and path	Years	Source files	Used for	Last modified (UTC)	Size of the source files
AlphaEarth Satellite Embedding, annual	V1; Source Cooperative `tge-labs/aef/v1/annual`	2017–2025	291 (4,049 blocks read)	all AlphaEarth analyses	2025-11-04 to 2026-03-22	0.84 TB
TESSERA annual representations	v1; Source Cooperative `tessera/tessera/npy/v1`	2017–2025	3,440 (embedding and scale files)	Emilia-Romagna, Fujian, Helene, Jishishan, Luding, Lushan, Mesetas	2026-06-24 to 2026-07-30	232.7 GB
TESSERA annual representations	v1.1-cam; `tessera/tessera/npy/v1.1-cam`	2017–2024	512	Agatha, Freddy, São Paulo; Mesetas (version check)	2026-08-12 to 2026-08-13	40.7 GB

File	SHA-256
AlphaEarth tile index (`aef_index.parquet`, 4 October 2026)	`f738e7d274ad582e56e20a3a8b444c6f2a3ece5781f8f9855bb7ca3d9ed2942f`
TESSERA manifest v1 (`manifest_v1.parquet`, 14 October 2026)	`b7d0717c20f3955b4832ee006aa6d835f18b3a376083f7616205add134246c5a`
TESSERA manifest v1.1-cam (`manifest_v1.1-cam.parquet`, 14 October 2026)	`3fc630a805a04f9789c07b1248aaf9541122944115abc3ffd99363ff3387c99a`
Supplementary Data S1 (AlphaEarth file list)	`5f4b94abb832c1f5673c06544dcebac024265f8b71571ee3aa18c50f1e40779d`
Supplementary Data S2 (TESSERA file list)	`bd8215543029419fb62c3247d8cb27bccc0c7dc4c3d194876a91ec53b95acbb2`

AUC aggregation, preprocessing and support sensitivities

Table S19

Annual AEF increments under pooled out-of-fold and within-fold pair-weighted AUC. Event rows are full-sample point estimates; within-fold intervals are paired spatial-cluster intervals. The primary bootstrap-mean event summaries remain in Table S2. No score calibration or spatial redesign is introduced.

Event	Point pooled	Point within-fold (95% CI)	Patch pooled	Patch within-fold (95% CI)
Chittagong	+0.1281	+0.108 (+0.090, +0.127)	+0.0903	+0.079 (+0.059, +0.100)
São Paulo	+0.1666	+0.166 (+0.104, +0.245)	+0.0876	+0.077 (+0.038, +0.132)
Fujian	+0.0687	+0.061 (+0.036, +0.095)	+0.0249	+0.026 (-0.004, +0.056)
Agatha	+0.1441	+0.132 (+0.106, +0.160)	+0.0927	+0.089 (+0.064, +0.115)
Freddy	+0.0583	+0.072 (+0.042, +0.098)	+0.0384	+0.059 (+0.035, +0.085)
Nalgae (Mindanao)	+0.0355	+0.021 (-0.003, +0.055)	-0.0146	-0.003 (-0.023, +0.011)
Luzon	+0.1996	+0.189 (+0.166, +0.217)	+0.2019	+0.190 (+0.166, +0.222)
Northern Vietnam	+0.1414	+0.133 (+0.099, +0.173)	+0.0862	+0.084 (+0.041, +0.122)
Lushan	+0.0912	+0.121 (+0.096, +0.153)	+0.0785	+0.123 (+0.088, +0.165)
Mesetas	+0.0061	+0.015 (+0.005, +0.026)	+0.0199	+0.017 (+0.003, +0.032)
Palu	+0.1149	+0.108 (+0.078, +0.148)	+0.1306	+0.124 (+0.079, +0.174)
Pasaman	+0.0896	+0.094 (+0.066, +0.134)	+0.0533	+0.057 (+0.034, +0.088)
Helene	+0.0733	+0.070 (+0.059, +0.082)	+0.0649	+0.058 (+0.049, +0.073)
Eastern Iburi	+0.0980	+0.095 (+0.074, +0.123)	+0.1178	+0.103 (+0.076, +0.133)
Jishishan	+0.0259	-0.010 (-0.028, +0.011)	-0.0173	-0.008 (-0.038, +0.026)
Luding	+0.0849	+0.044 (+0.037, +0.058)	+0.1072	+0.065 (+0.048, +0.090)
Mangkhut	+0.0551	+0.055 (+0.040, +0.074)	+0.1073	+0.083 (+0.045, +0.128)
Emilia-Romagna	+0.0248	+0.037 (+0.029, +0.047)	+0.0155	+0.031 (+0.026, +0.039)

The arithmetic event average and random-effects summary are different quantities. The latter uses each event's bootstrap mean and standard error, as in the retained principal estimator.

Model	AUC aggregation	Event arithmetic mean	Random-effects mean (95% CI)	Positive events
CNN2D	pooled	0.0714	+0.070 (+0.048, +0.093)	16/18
CNN2D	within	0.0697	+0.069 (+0.050, +0.088)	16/18
LightGBM	pooled	0.0892	+0.087 (+0.065, +0.110)	18/18
LightGBM	within	0.0840	+0.082 (+0.062, +0.103)	17/18

Table S20

Optical seasonal comparison under both AUC aggregations. The absolute levels average ten separately evaluated three-date draws; all confidence intervals use paired spatial and draw resampling. The common supports contain 281/972 positives/controls at Iburi and 315/442 at Mangkhut.

Event	Year / cutoff (days)	Pooled AUC (95% CI)	Within-fold AUC (95% CI)
Eastern Iburi	2017 / -1	0.429 (0.381, 0.485)	0.533 (0.493, 0.577)
Eastern Iburi	2017 / 60	0.397 (0.355, 0.450)	0.490 (0.450, 0.528)
Eastern Iburi	2018 / -1	0.420 (0.373, 0.480)	0.551 (0.510, 0.588)
Eastern Iburi	2018 / 60	0.811 (0.762, 0.847)	0.844 (0.768, 0.881)
Mangkhut	2017 / -1	0.516 (0.469, 0.554)	0.549 (0.493, 0.603)
Mangkhut	2017 / 60	0.596 (0.549, 0.635)	0.616 (0.570, 0.670)
Mangkhut	2018 / -1	0.475 (0.437, 0.515)	0.525 (0.486, 0.566)
Mangkhut	2018 / 60	0.786 (0.755, 0.814)	0.783 (0.746, 0.824)

Seasonal excess: [2018 (+60 minus -1 day)] minus [2017 (+60 minus -1 day)].

Event	Pooled (95% CI)	Within-fold (95% CI)	Equal-fold point estimate
Eastern Iburi	+0.423 (+0.353, +0.479)	+0.335 (+0.255, +0.402)	0.283
Mangkhut	+0.231 (+0.164, +0.293)	+0.191 (+0.117, +0.260)	0.169

Event	Positive counts in folds 0–4	Control counts in folds 0–4
Eastern Iburi	46, 102, 120, 9, 4	295, 122, 158, 205, 192
Mangkhut	34, 133, 97, 2, 49	143, 101, 99, 72, 27

Small positive folds contribute few sample pairs to the pair-weighted statistic. Its difference from pooled AUC reflects the excluded cross-fold pairs and potentially different model score scales; it is not attributed solely to calibration. The lower pooled pre-event Iburi level therefore does not establish absence of pre-event information.

Table S21

AEF patch missingness and the targeted imputation sensitivity. The first table summarizes all 69 primary event-year arrays across 18 events after original eligibility. The maximum is taken across an event's available primary years; the accompanying CSV gives every event-year, before and after eligibility, plus class/fold counts. A spatial cell is missing if any of its 64 channels is NaN; a patch is affected if any cell is missing. No infinite values were found.

Event	Primary years scanned	Max missing values (%)	Max missing cells (%)	Max affected patches (%)
Chittagong	2021, 2022, 2023, 2024	0.3338	0.3338	1.302
São Paulo	2021, 2022, 2023, 2024	0.0380	0.0380	0.139
Fujian	2021, 2022, 2023, 2024	0.0000	0.0000	0.000
Agatha	2020, 2021, 2022, 2023	0.0000	0.0000	0.000
Freddy	2021, 2022, 2023, 2024	0.0595	0.0595	0.218
Nalgae (Mindanao)	2020, 2021, 2022, 2023	0.0000	0.0000	0.000
Luzon	2021, 2022, 2023, 2024	0.1094	0.1094	0.387
Northern Vietnam	2021, 2022, 2023, 2024	0.0221	0.0221	0.101
Lushan	2020, 2021, 2022, 2023	0.1602	0.1602	0.648
Mesetas	2017, 2018, 2019, 2020	0.1766	0.1766	0.704
Palu	2017, 2018, 2019	0.0338	0.0338	0.307
Pasaman	2020, 2021, 2022, 2023	0.0000	0.0000	0.000
Helene	2022, 2023, 2024, 2025	0.0849	0.0849	0.377
Eastern Iburi	2017, 2018, 2019	0.3006	0.3006	1.203
Jishishan	2021, 2022, 2023, 2024	0.0522	0.0522	0.205
Luding	2020, 2021, 2022, 2023	0.1746	0.1746	0.680
Mangkhut	2017, 2018, 2019	0.3554	0.3554	1.212
Emilia-Romagna	2021, 2022, 2023, 2024	0.1232	0.1232	0.507

Mangkhut was selected by maximum retained missing-cell fraction before refitting. Both 2017 and 2018 have 1,419/399,300 missing cells (0.3554%), affecting 40/3,300 patches (1.212%). Thirty fold/year/seed jobs each fit the two operators, for 60 fits in total; all settings except imputation are paired.

Operator / comparison	Annual AUC increment (95% CI)
Archived prediction	+0.107 (+0.056, +0.157)
Re-fit: global channel mean	+0.107 (+0.056, +0.157)
Re-fit: inner fitting mean	+0.110 (+0.058, +0.160)
Change in annual increment	+0.0024 (+0.0003, +0.0045)

The paired change is +0.00237 (0.00030, 0.00452). It remains below the locally specified 0.01 trigger for considering more events; no additional CNN events were retrained. This check quantifies one deliberately selected high-missingness case. Intervals condition on these refits. The archive contains both raw Mangkhut patch arrays, inner training/validation indices, channel means, per-seed scores and the exact training implementation.

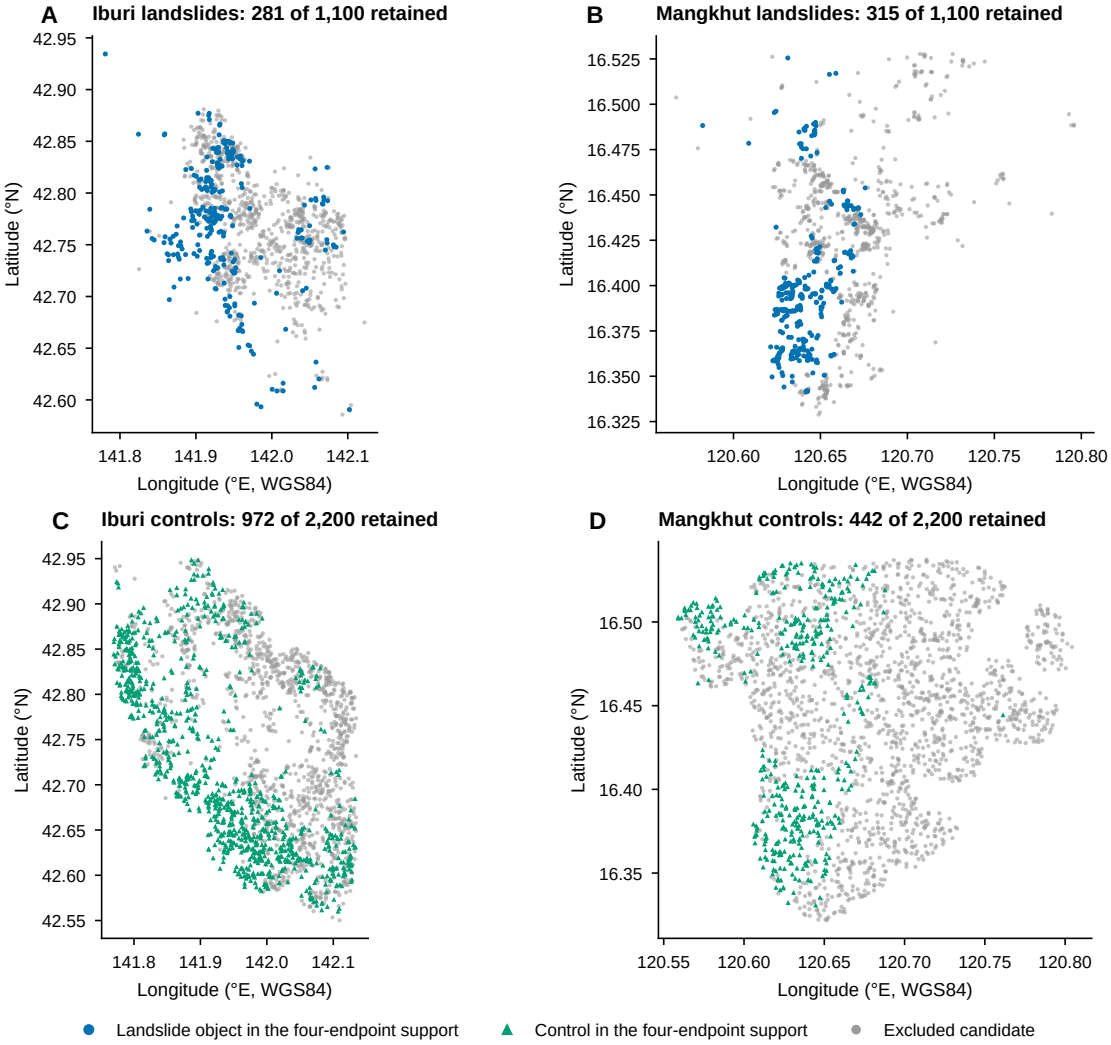


Fig. S1. Optical support selection. Landslide points represent unique inventory objects; controls are shown in separate panels. Coloured symbols mark candidates retained in the principal four-endpoint seasonal comparison (blue circles, landslide objects; green triangles, controls); grey dots mark excluded candidates. The full flow, intersections and selection-variable distributions accompany the archive.

Table S22

Composition of the four-endpoint seasonal common support. Retention fractions use the same initial candidate set within each event and class. GLO-30 local slope is a descriptive summary; its valid counts are supplied in the CSV. All candidates have known WorldCover 2021 v200 classes. "Tree cover" is WorldCover class 10; the complete class distribution is supplied as counts and proportions, including zero-count classes. The 2021 description is later than the 2018 events and does not represent pre-event cover.

Event	Class	Retained / candidate	Slope retained / excluded (°)	Tree cover retained / excluded (%)
Eastern Iburi	Landslide	281/1100 (25.5%)	18.7 / 22.3	66.2 / 71.3
Eastern Iburi	Control	972/2200 (44.2%)	12.5 / 17.6	90.3 / 93.4
Mangkhut	Landslide	315/1100 (28.6%)	31.6 / 31.7	74.6 / 51.8
Mangkhut	Control	442/2200 (20.1%)	23.4 / 28.0	85.7 / 76.5